NeuroImage 270 (2023) 119944

Contents lists available at ScienceDirect

NeuroImage

journal homepage: www.elsevier.com/locate/neuroimage

Identification of overlapping and interacting networks reveals intrinsic spatiotemporal organization of the human brain

Jian Li[a,b], Yijun Liu[c], Jessica L. Wisnowski[d,e,1], Richard M. Leahy[c,1,*]

[a] Athinoula A. Martinos Center for Biomedical Imaging, Massachusetts General Hospital and Harvard Medical School, Charlestown, MA, USA
[b] Center for Neurotechnology and Neurorecovery, Department of Neurology, Massachusetts General Hospital and Harvard Medical School, Boston, MA, USA
[c] Ming Hsieh Department of Electrical and Computer Engineering, University of Southern California, Los Angeles, CA, USA
[d] Radiology and Pediatrics, Division of Neonatology, Children's Hospital Los Angeles, Los Angeles, CA, USA
[e] Keck School of Medicine, University of Southern California, Los Angeles, CA, USA

ARTICLE INFO

Keywords:
Brain network identification
Functional connectivity
Spatiotemporal organization
Temporal synchronization
Tensor decomposition

ABSTRACT

The human brain is a complex network that exhibits dynamic fluctuations in activity across space and time. Depending on the analysis method, canonical brain networks identified from resting-state fMRI (rs-fMRI) are typically constrained to be either orthogonal or statistically independent in their spatial and/or temporal domains. We avoid imposing these potentially unnatural constraints through the combination of a temporal synchronization process ("BrainSync") and a three-way tensor decomposition method ("NASCAR") to jointly analyze rs-fMRI data from multiple subjects. The resulting set of interacting networks comprises minimally constrained spatiotemporal distributions, each representing one component of functionally coherent activity across the brain. We show that these networks can be clustered into six distinct functional categories and naturally form a representative functional network atlas for a healthy population. This functional network atlas could help explore group and individual differences in neurocognitive function, as we demonstrate in the context of ADHD and IQ prediction.

1. Introduction

The human brain is a complex network that exhibits dynamic fluctuations in activity across space and time, even at rest. Characterizing this spatiotemporal architecture and how variations across the population explain individual differences in neurocognitive functions is a central question in neuroscience.

More than two decades ago, scientists first observed that, at rest, the brain exhibits coherent fluctuations in blood oxygenation level dependent (BOLD) signaling – measured by functional MRI (fMRI) – across distributed regions in the human brain (Fox and Raichle, 2007). From these coherent fluctuations, a canonical set of large-scale resting-state networks have emerged, including the default mode, visual, somatomotor, salience, attention, and executive control networks (Uddin et al., 2019). Evidence suggests that neurocognitive dysfunction can be at least partially understood as an imbalance of activity within and across these networks (Bressler and Menon, 2010). Although multiple networks are identifiable and highly reproducible across task and resting-state fMRI (rs-fMRI) studies, the computational methods used in their identification have frequently relied on assumptions of orthogonality or statistical independence (Calhoun et al., 2001) that are driven more by their appealing mathematical properties than our understanding of brain networks. As a result, we may inadvertently constrain the characteristics of identified networks and consequently, our understanding of the human connectome.

Two distinct approaches to the identification of brain networks are described in the literature: (i) those based on spatial decompositions in which each network is represented as an image reflecting the participation of each voxel; (ii) those based on parcellation in which the brain is partitioned into a set of non-overlapping functionally homogeneous regions. In the former group, (spatial) independent component analysis (ICA) is most often used and usually applied to temporally concatenated data from individuals with an independence constraint in the spatial domain (Calhoun et al., 2001). Although many meaningful components can be extracted using these ICA-based approaches (Calhoun et al., 2009), the estimated spatial maps are constrained to be statistically independent. Principle component analysis (PCA)-based and dictionary learning-based approaches have also been proposed (Dadi et al., 2020; Smith et al., 2014), yet they impose either orthogonality or sparsity constraint instead of independence, which also may not be physiologically plausible. The latter approach is exemplified in work by Yeo and colleagues, who parcellated the human cortex based

* Corresponding author.
E-mail address: leahy@sipi.usc.edu (R.M. Leahy).
[1] Co-senior authors.

https://doi.org/10.1016/j.neuroimage.2023.119944.
Received 9 July 2022; Received in revised form 6 January 2023; Accepted 14 February 2023
Available online 19 February 2023.

on the Pearson correlation of rs-fMRI time-series (Yeo et al., 2011). Follow-up studies extended the parcellation framework to whole-brain (Craddock et al., 2012), a larger number of parcels (Schaefer et al., 2018), or multi-modal datasets (Glasser et al., 2016). The parcellation approach emphasizes functional homogeneity within each parcel and explicitly prohibits spatial overlap. Therefore, a contiguous cortical region that is fully involved in one network but only a portion of which is involved in a second needs to be represented by two parcels. This leads to the need for very dense parcellations to accommodate overlapping networks. An alternative is to use a sliding-window framework for identification of quasi-stationary brain macro-states using methods based on k-means clustering (Allen et al., 2014), graph analysis (Tagliazucchi et al., 2012), or dictionary learning (Leonardi et al., 2014). However, these methods assume the brain is in a single "state" at each time point, so in contrast to the spatial parcellation methods, these methods perform a non-overlapping parcellation in time.

Functional connectivity has been shown to fluctuate over time in a manner that is more complex than the discrete macro-state mode (Hutchison et al., 2013; Karahanoğlu and Van De Ville, 2015; Tagliazucchi et al., 2012). Assumptions of stationarity in time may therefore be too restrictive to capture the dynamic nature of the brain (Rabinovich et al., 2012). On the other hand, spatial overlap between large-scale brain networks has been widely observed in fMRI data (Karahanoğlu and Van De Ville, 2015; Xu et al., 2016; Yeo et al., 2014), and the nomenclature of large-scale brain networks still remains controversial (Uddin et al., 2022, 2019). Supporting evidence shows that cortical brain activities are not segregated in space. Rather, they overlap and interact with each other at different scales, which could potentially be attributed to the heterogeneous activity of intermingled neurons within the same brain region (Harris and Mrsic-Flogel, 2013). Specifically, the laminar organization of the cerebral cortex combines a hierarchical structure with a high degree of parallel processing (Rockland, 2019). The extrinsic connections to and from the cerebral cortex target specific cortical layers depending on the loci of origin and termination, and the hierarchical relationship between the regions. This microstructural organization suggests that at a macroscale, cortical and subcortical regions should interact across multiple networks superimposed across space and time. Recently, emerging studies have focused on identifying overlapping and correlated brain networks. For example, Harrison et al. developed a complex Bayesian model to describe brain networks considering both a group prior and inter-subject variations (Harrison et al., 2015). Later extensions include modeling of network interactions and stochastic inference that can be scaled to very large datasets (Farahibozorg et al., 2021; Harrison et al., 2020). However, as with ICA or PCA, these approaches do not exploit any *intrinsic* low-rank structure embedded directly in higher dimension space for group analysis as we do using a tensor model below.

In this work, we define a brain network as a functional component that *jointly describes both spatial distribution and temporal variations*, where *neither the spatial nor temporal domain is unrealistically constrained*. In contrast to the traditional network terminology, e.g., the default mode network, where only the spatial map is well characterized, this renewed definition could help us explore a fundamental question in functional connectivity analysis: which parts of the brain ("where") talk to each other at which given period of time ("when").

We approach this network identification problem using a combination of the BrainSync algorithm (Akrami et al., 2019; Joshi et al., 2018a) and the Nadam-Accelerated SCAlable and Robust (NASCAR) tensor decomposition method (Li et al., 2019b, 2021). We identified twenty-three brain networks using rs-fMRI data from a large group of healthy subjects acquired by the Human Connectome Project (HCP) (Glasser et al., 2013; Van Essen et al., 2012). These networks are spatially overlapped, temporally correlated, and highly reproducible across two independent groups and sessions. We also show that these networks can be clustered into six distinct functional categories. The spatiotemporal organization of these brain networks naturally forms a representative functional atlas for the healthy population, which can be used to explore group and individual differences in neurocognitive function, as we demonstrate in the context of attention deficit hyperactivity disorder (ADHD) and Intelligence Quotient (IQ) prediction.

2. Material and methods

2.1. The human connectome project dataset

We used the minimally preprocessed 3T resting-state fMRI (rs-fMRI) data from 1000 subjects (466 males, 534 females, age between 22 and 35) in the publicly available Human Connectome Project (HCP) database (Glasser et al., 2013; Van Essen et al., 2012). Each subject has two sessions of scans with two different phase encoding directions (LR, RL). We used both sessions from the LR direction only to minimize inter-subject misalignment due to residual differences in EPI distortion with phase-encoding direction after correction during preprocessing (Smith et al., 2013). These data were acquired with $TR = 720$ ms, $TE = 33.1$ ms and a 2 mm isotropic resolution and co-registered onto a common atlas in MNI space. Each session ran 15 min, with 1200 frames in total. The data were resampled onto the cortical surface extracted from each subject's T1-weighted MRI and co-registered to a common surface (Glasser et al., 2013). The spatial dimension was further downsampled by a factor of three for computational tractability, where there are approximately 22 K vertices across the two hemispheres. We note that no predefined atlas was used, and the following studies were performed directly at the voxel level in the grayordinate system. We also note that no additional spatial smoothing was applied beyond the 2 mm full width half maximum isotropic Gaussian smoothing used in the minimal preprocessing pipeline (Glasser et al., 2013) because linear smoothing can blur boundaries between functional regions (Li et al., 2018, 2020a; Li and Leahy, 2017).

2.2. The ADHD-200 datasets

We evaluated all 259 subjects from Peking University in the ADHD-200 dataset (The ADHD-200 Consortium, 2012). We excluded subjects with incomplete evaluations or measures, such as ADHD index based on their phenotypic information. The total number of subjects with complete data was 221 (159 males, 62 females, age 11.7 ± 2.0), with 95 diagnosed as having ADHD and the remaining 126 were neurotypical (NT). The rs-fMRI data were recorded using a Siemens Trio 3T scanner with a $TR = 2$ s. We preprocessed the rs-fMRI data using our in-house BrainSuite functional Pipeline (BFP) (http://brainsuite.org/bfp/) (Joshi et al., 2018b). BFP uses a series of scripts from AFNI (Cox, 1996), BrainSuite (Shattuck and Leahy, 2002), and FSL (Jenkinson et al., 2012) to minimally preprocess rs-fMRI data. After applying BFP, the rs-fMRI data were co-registered and re-sampled onto the same tessellated surfaces as used with the HCP dataset. We identified eleven outliers based on Cook's distance metric: a linear regression model was fit to the ADHD index using the estimated subject participation level described below. Then the Cook's distance was measured for each subject. Subjects who had a Cook's distance higher than the standard threshold $4/N$ ($N = 221$, the total number of subjects) (Van der Meer et al., 2010) were identified as outliers and excluded from further study.

2.3. Brain network identification pipeline and its application to the HCP dataset

The blood-oxygen-level-dependent (BOLD) signals in rs-fMRI data from different subjects are not temporally locked, hence not directly comparable in time. However, the low-rank tensor model described below requires temporal synchrony across subjects. We used the BrainSync algorithm to achieve temporal alignment of the rs-fMRI data (Joshi et al., 2018a). BrainSync finds an optimal temporal orthogonal

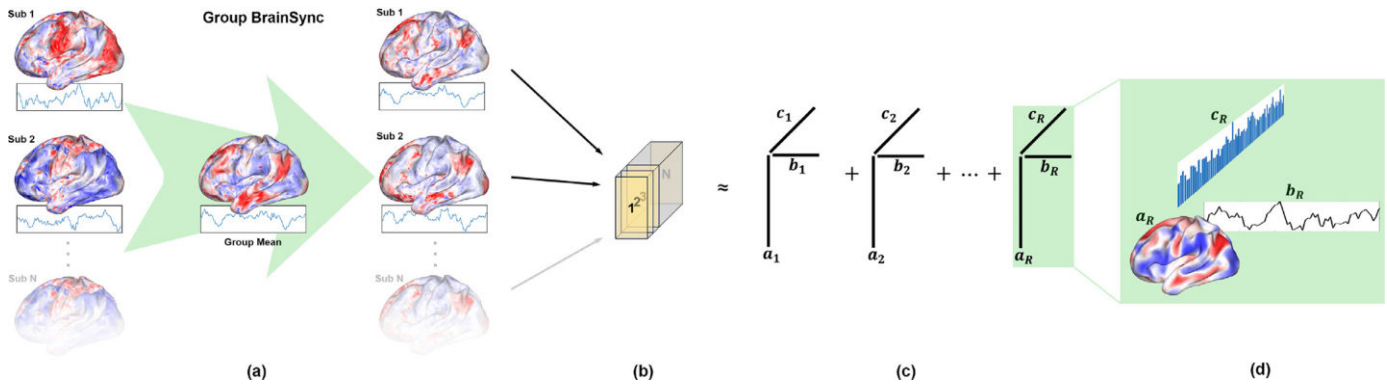

Fig. 1. Brain network identification from group rs-fMRI. (a) Resting-state data are temporally synchronized to a group mean using Group BrainSync; (b) a third-order tensor is formed with subject-index as the third dimension; (c) NASCAR tensor decomposition; (d) Visualization of the spatial map ($\boldsymbol{a}_i$), temporal variations ($\boldsymbol{b}_i$), and subject participation level ($\boldsymbol{c}_i$).

transformation between two subjects, such that the time series in homologous regions of the brain are highly correlated after synchronization. To avoid potential bias in the selection of the specific reference subject, we used the group version of the BrainSync algorithm (Akrami et al., 2019) to build a virtual reference subject, which is closest, in the mean-square sense, to all subjects. We then temporally aligned all subjects' data to the virtual reference to obtain a multi-subject synchronized dataset, as shown in Fig. 1(a). Let $\boldsymbol{X} \in \mathbb{R}^{V\times T}$ be the synchronized rs-fMRI data of an individual subject, where $V \approx 22K$ is the number of vertices (space) and $T = 1200$ is the number of time points (time). Then all subjects were concatenated along the third dimension (subject), forming a data tensor $\mathcal{X} \in (\mathbb{R})^{V\times T\times S}$, where S is the number of subjects, Fig. 1(b). We model brain networks present in the group rs-fMRI data as a low-rank Canonical Polyadic (CP) model, Fig. 1(c):

$$\boldsymbol{\mathcal{X}} \approx \sum_{r=1}^{R} \lambda_r \, \boldsymbol{a}_r \circ \boldsymbol{b}_r \circ \boldsymbol{c}_r \tag{1}$$

where each component $\lambda_i \, \boldsymbol{a}_i \circ \boldsymbol{b}_i \circ \boldsymbol{c}_i$ represents a brain network; $\boldsymbol{a}_i \in \mathbb{R}^V$, $\boldsymbol{b}_i \in \mathbb{R}^T$, and $\boldsymbol{c}_i \in \mathbb{R}^S$ are the spatial map, the temporal variations, and the subject participation level, respectively, in the i^{th} network, Fig. 1(d); λ_i represents the 'strength' of the network, indicating the magnitude of activity relative to other networks averaged across all subjects. Each of the components $\boldsymbol{a}_i$, $\boldsymbol{b}_i$, $\boldsymbol{c}_i$ are normalized to unit length within the NASCAR algorithm. The Rank R represents the desired maximum number of networks. $R = 50$ was used in this work as a reasonable upper bound based on the rank of rs-fMRI reported in the literature (Biswal et al., 2010; Calhoun et al., 2001; Harrison et al., 2020).

An interesting property of the CP model is that the decomposition is generally unique under mild conditions. For tensors of order 3 or higher, the condition

$$\mathrm{k}_{\boldsymbol{A}} + \mathrm{k}_{\boldsymbol{B}} + \mathrm{k}_{\boldsymbol{C}} \geq 2R + 2 \tag{2}$$

is sufficient (Kruskal, 1989, 1977; Sidiropoulos and Bro, 2000) and necessary (ten Berge and Sidiropoulos, 2002) for the CP decomposition in Eq. (1) to have a unique solution. Here $\boldsymbol{A} = [\boldsymbol{a}_1 \; \boldsymbol{a}_2 \cdots \boldsymbol{a}_R] \in \mathbb{R}^{V\times R}$ are the concatenated factors along the first dimension, $k_{\boldsymbol{A}}$ is the column rank of $\boldsymbol{A}$, and similarly for $\boldsymbol{B} \in \mathbb{R}^{T\times R}$ and $k_{\boldsymbol{B}}$ and for $\boldsymbol{C} \in \mathbb{R}^{S\times R}$ and $k_{\boldsymbol{C}}$. In contrast to PCA and ICA, no orthogonality or statistical independence assumptions are placed on the components of the decomposition. It is this change in the setting of the problem from a 2D (ICA, PCA) to 3D (CP) decomposition that allows us to lift the orthogonality or independence constraint, which may not be physiologically plausible for brain networks.

We solved the CP decomposition in Eq. (1) using the Nadam-Accelerated SCAlable and Robust (NASCAR) canonical polyadic decomposition algorithm (Li et al., 2019b, 2021). NASCAR employs an iterative method using low-rank solutions as part of the initializations when solving higher-rank problems. The robustness of the solutions and the scalability to a large dataset is substantially improved by using this warm start approach. Its performance relative to other network identification methods has been demonstrated in applications to both electroencephalography (EEG) data (Li et al., 2019a, 2017) and task fMRI data (Li et al., 2021, 2019b). Here we randomly divided the 1000 HCP subjects into two equally sized groups and applied this pipeline to the rs-fMRI data for each group and each session independently (2 groups × 2 sessions = 4 sessions in total).

2.4. Simulation

For each simulated experiment, we generated a third-order tensor $\boldsymbol{\mathcal{X}} \in (\mathbb{R})^{100\times 100\times 10}$ with a rank of $R = 3$ to mimic a real data scenario. The data were randomly generated based on zero mean and unit variance multivariate normal distributions. The spatial modes were correlated between the first and second components. The temporal modes were correlated between the first and third components. The subject mode was non-negative for all components. We simulated four different correlation structures: 1) Low spatial and temporal correlations ($r_{spatial} = r_{temporal} = 0.2$); 2) High spatial correlation but low temporal correlation ($r_{spatial} = 0.8$, $r_{temporal} = 0.2$); 3) Low spatial correlation but high temporal correlation ($r_{spatial} = 0.2$, $r_{temporal} = 0.8$); and 4) High spatial and temporal correlations ($r_{spatial} = r_{temporal} = 0.8$). Independent random Gaussian noise was added with a signal-to-noise ratio of 0.05, which was chosen empirically so that the measured performance would not be saturated.

We ran each simulated experiment 100 times using both NASCAR and group spatial ICA (sICA) (Calhoun et al., 2001). We evaluated the performance using the averaged congruence product (ACP) (Tomasi and Bro, 2005). ACP is a measure of the averaged correlation between components defined as

$$ACP = \max_{\boldsymbol{P}} \frac{1}{R} tr\left(\left(\boldsymbol{A}^T \hat{\boldsymbol{A}}\right) * \left(\boldsymbol{B}^T \hat{\boldsymbol{B}}\right) \boldsymbol{P}\right) \tag{3}$$

where $\boldsymbol{A}$ and $\boldsymbol{B}$ are the ground truth spatial and temporal mode, and $\hat{\boldsymbol{A}}$ and $\hat{\boldsymbol{B}}$ are their estimated counterparts, $\boldsymbol{P}$ is a permutation matrix accounting for the ambiguity of the ordering of the solutions (Harshman, 1970) and tr is the trace of a matrix.

2.5. Post-NASCAR processing: spectrum estimation, network matching, and recognition

While correlations are unaffected by the orthogonal BrainSync transform, the virtual reference space does not itself provide time series that can be interpreted with respect to their temporal variations or frequency content. Consequently, for visualization and spectral analysis, we applied the inverse-BrainSync transform of the temporal variations ($\boldsymbol{b}_i$)

for each network to an arbitrary default subject (subject 100,307 in the HCP dataset). The power spectrum of the inversed time series was then estimated using the Welch method (Welch, 1967) with 24 50% overlapped Hamming windowed segments, each of length 100.

As with other data-driven approaches (e.g., ICA, Kelly et al., 2010), we manually examined the NASCAR components based on their spatial maps, estimated spectra, and subject participation level to identify artifactual components. In total, 17 components were identified as artifact or noise and removed from further consideration, Fig. S1. Of these, 7 had only one or a few subjects with high participation levels and 10 exhibited physiologically-implausible "noise" components.

To enable comparison of components across sessions, networks from all other sessions were matched to the first group's first session using the Gale-Shapley algorithm (Gale and Shapley, 1962). This algorithm requires an equal number of networks in each session. Each network is assigned its best match. If there is a strong one-to-one correspondence between networks in two sessions with only an ordering difference, Gale-Shapley will find the correct match. However, if one or more of the components do not match well between sessions, the resulting matches will be poorly correlated. In the following we therefore selected the twenty-three most reproducible components in the decomposition by thresholding the maximum of the inter-session correlations across all pairs of sessions at 0.9, as shown in the supplementary Fig. S2.

To label the likely functionality of these networks, we computed Pearson cross-correlation matrices using the spatial ($\boldsymbol{a}_i$), temporal ($\boldsymbol{b}_i$), subject mode ($\boldsymbol{c}_i$), and estimated spectra. By jointly visualizing the spatial, temporal, and subject mode as well as structures and patterns in the four cross-correlation matrices, we manually clustered the networks into six functional categories and ordered them based on the cluster categories, as shown in Fig. 5. Specifically, visual, auditory, and sensorimotor networks can be easily recognized from the regions of cortical activation visible in the spatial maps. By comparing the spatial maps with the literature, it is also straightforward to identify default mode networks (DMN), where posterior cingulate cortex (PCC), medial prefrontal cortex (mPFC), and inferior parietal lobule (IPL) are the core hubs. Relying on our knowledge that task-positive networks are anti-correlated with DMNs, we identified the higher-order cognitive (HOC) networks based on the temporal correlation matrix. Finally, the global signals exhibit a distinct spectral peak at 0.3 Hz. All four are highly correlated with each other in both time and spectrum.

We also ran the group sICA algorithm (Calhoun et al., 2001) on the same dataset and repeated the network identification and clustering procedure. For each session and group, 50 networks were identified, and the temporal variations were then back-reconstructed using dual regression (Calhoun et al., 2009, 2001). The cross-correlation matrices were computed with identical methods and parameters as for NASCAR. 23 highly consistent networks across 4 total sessions were identified after network matching. The entire analysis pipeline for ICA was performed identically but independently of the NASCAR pipeline described above for a meaningful comparison.

2.6. Building a functional network atlas and estimation of subject participation level for independent dataset

In contrast to brain atlases where the brain is parcellated into many spatially contiguous, non-overlapping, and hopefully functionally distinct and homogenous regions, the networks identified by the NASCAR method above using the large HCP dataset naturally form a spatiotemporal atlas that jointly describes overlapped spatial maps and correlated temporal variations, which we refer to as a *functional network atlas*. Here we illustrate two of the many potential applications of this atlas via 1) an rs-fMRI study of ADHD subjects and 2) prediction of Intelligence Quotient (IQ) in a healthy population.

For the ADHD study, we used independent rs-fMRI data acquired from Peking University as part of the ADHD-200 dataset (The ADHD-200 Consortium, 2012), as described in Section 2.2. The functional network atlas built from the HCP dataset could be reformed into a set of bases by vectorizing the outer product of the spatial map and the temporal variations of each network. Specifically, let $\boldsymbol{g}_i = vec(\boldsymbol{a}_i \circ \boldsymbol{b}_i)$, where $vec(\cdot)$ is the vectorization operator. Then $\boldsymbol{G} = [\boldsymbol{g}_1, \boldsymbol{g}_2, \ldots, \boldsymbol{g}_R] \in \mathbb{R}^{VT\times R}$ forms the network atlas bases. Let $\boldsymbol{Y} \in \mathbb{R}^{V\times T}$ be any rs-fMRI single-subject data, independent from that used to compute the atlas (in this case, the ADHD data). Then the subject participation level for this subject can be estimated by a least-square fit: $\boldsymbol{c} = \boldsymbol{G}^{\dagger}\boldsymbol{y} \in \mathbb{R}^{R\times 1}$, where $\boldsymbol{y} = vec(\boldsymbol{Y}) \in \mathbb{R}^{VT\times 1}$, $\boldsymbol{G}^{\dagger}$ is the pseudo inverse of $\boldsymbol{G}$. In this way, the resulting subject participation levels embed the intrinsic properties of the brain networks for each subject using the network atlas.

The concatenation of participation levels from all subjects in the ADHD dataset forms a feature matrix $\boldsymbol{C} \in \mathbb{R}^{N\times R}$, where N is the number of subjects and R is the number of networks. To demonstrate the effectiveness of information extraction from the rs-fMRI data, we first treated the feature matrix $\boldsymbol{C}$ as a group of column vectors as shown in Fig. 6(a) below (left arrow). We then used these column vectors as bases to predict the ADHD index using linear regression with 10-fold cross-validation. We next used the row vectors in feature matrix $\boldsymbol{C}$, as shown in Fig. 6(a) (right arrow), as features to differentiate ADHD from NT. Specifically, we trained a binary support vector machine (SVM) (Cortes and Vapnik, 1995) using the ground truth label (we do not consider sub-types here) to classify ADHD and NT. Lastly, to illustrate how activity in these networks differs between ADHD and NT, we took the average subject participation level in each of the six network categories for ADHD and NT separately and computed their medians and standard errors. The results were normalized globally to have a maximum (median) of 1 and a minimum of 0.5 for visualization.

We repeated the ADHD study using group sICA, PCA, and a parcellation-based method. Since sICA does not provide a common temporal mode for the group, the subject participation levels in sICA cannot be obtained by a direct projection of the ADHD data to the spatiotemporal atlas as for NASCAR. Instead, we built a spatial atlas using the 23 identified reproducible sICA networks as described in Section 2.5. The individual temporal mode was then obtained by a projection of individual ADHD subject data onto the spatial atlas (as with the dual regression). The subject participation level for each subject was then estimated as the norm of the temporal mode. For PCA, we used the 23 components that have the largest singular values and hence explain the most variance in the HCP data. The subject participation levels were similarly estimated as with sICA. For the parcellation method, we used the Yeo-17 parcellation scheme, which is among the most widely used parcellations and comparable to ours in terms of the number of networks (parcels). We treated the binary network maps as spatial modes and obtained the temporal mode for each network as the time series averaged over the corresponding parcel. The subject modes were then estimated as the norm of the temporal mode for each network and each subject in the ADHD dataset. In addition to using these norms as features, we also explored the question of whether the more frequently used subject-specific functional connectivity from the ICA-dual regression time series (Liu et al., 2019; Nickerson et al., 2017) would produce improved ADHD score prediction. For this purpose, we used the lower triangle portion of the temporal correlation matrix between networks as features and repeated the ADHD index prediction study above. In this case the number of features is substantially larger than when using the norms of the temporal model, so we used ridge and lasso regression to prevent potential overfitting. Regularization parameters were determined using nested cross-validation.

The second application focuses on the prediction of IQ among the 1000 healthy subjects in the HCP database. To ensure independence between atlas building and IQ prediction, we used the atlas built from a group of 500 subjects and then estimated the subject participation levels for each subject in the second group of 500 subjects. The three IQ measures provided by the HCP (Van Essen et al., 2012) are Fluid IQ, indicating the ability to reason and digest newly acquired knowledge, Crystallized IQ, reflecting already accumulated

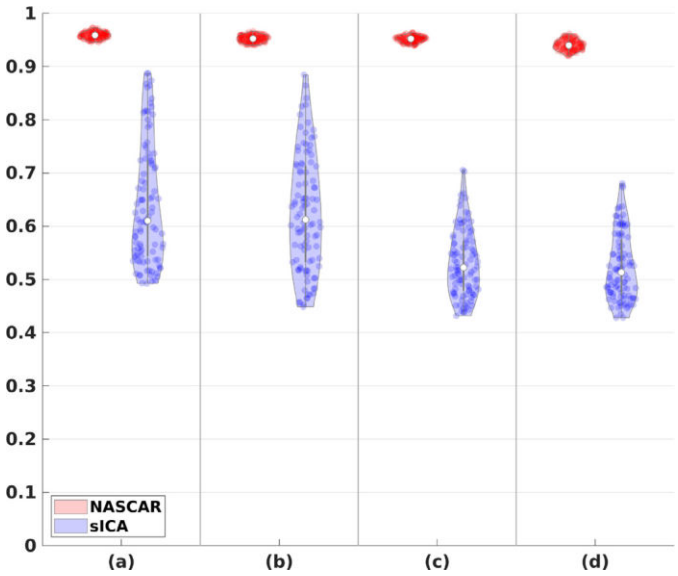

Fig. 2. Averaged congruence product (ACP) using NASCAR and sICA on simulated dataset. (a) Low spatial and temporal correlations; (b) Low spatial but high temporal correlations; (c) High spatial but low temporal correlations; (d) High spatial and temporal correlations.

knowledge, facts, and skills, and Total IQ, a weighted combination of the two.

The estimation of subject participation levels and the prediction procedure using cross-validated linear regression models were all identical to that in the ADHD study above. The analysis was performed and compared using NASCAR, sICA, PCA, and the Yeo-17 parcellated atlas.

3. Results

3.1. Simulation

Fig. 2 shows the ACP (Eq. (3)) for NASCAR in red and sICA in blue under the four different correlation scenarios. Overall, the ACP using NASCAR is substantially higher than that using sICA in all cases. This is because spatial correlation breaks the independence assumption present in ICA but not in NASCAR. Further, as expected, higher correlation in the spatial mode significantly reduces the performance for sICA as shown in (c, d) when compared with (a, b), and higher temporal correlation has minimal impact as shown in (b) compared with (a) and (d) compared with (c).

3.2. Highly reproducible brain networks were identified from resting-state fMRI data

Figs. 3 and 4 show the identified twenty-three networks grouped by their functional categories. Figs. S3 and S4 show the same set of networks with inflated surface representations. Three networks, Fig. 3(a) – (c), included the core regions of the canonical DMN: mPFC, precuneus, PCC, IPL, and lateral temporal cortex (LTC). Spatially, these networks displayed distinct features: Network (a) showed the strongest coherence between the dorsomedial (dm)-PFC, rostral IPL, LTC, and the inferior frontal gyrus (IFG). In contrast, network (b) showed the strongest coherence between the medial PFC, precuneus/PCC, and caudal temporoparietal junction (TPJ). Network (c) showed strong spatial overlap with both (a) and (b) but with an opposite sign between the left and the right hemispheres. All three networks had positive temporal correlations with each other and showed a strong correlation in the subject mode, Fig. 5(d). We also note that these networks appear to operate at different frequencies: (a) has a higher peak frequency (0.027 Hz) relative to (b) and (c) (0.011 Hz). Overall, the patterns suggest that (a) and (b) may represent sub-networks of the canonical DMN. To visually verify this observation, we combined (a) and (b) into a single network by 1) linearly scaling the spatial maps of (a) and (b) independently onto [0, 1]; 2) creating an RGB image where the scaled map of (a) was embedded as the red channel and the counterpart of (b) as the blue channel; 3) thresholding the red and blue channel data independently at 0.65 and setting the RGB triplet to white ([1,1,1]) for each vertex if both the red and the blue channel fell below this threshold so as to highlight the DMN active regions for visualization purpose. We observed that the merged network strongly resembles the canonical DMN, Fig. 3(d).

Three networks, Fig. 4(a) – (c), included core regions of the somatomotor cortices. Networks (a) and (b) centered on the face/tongue and

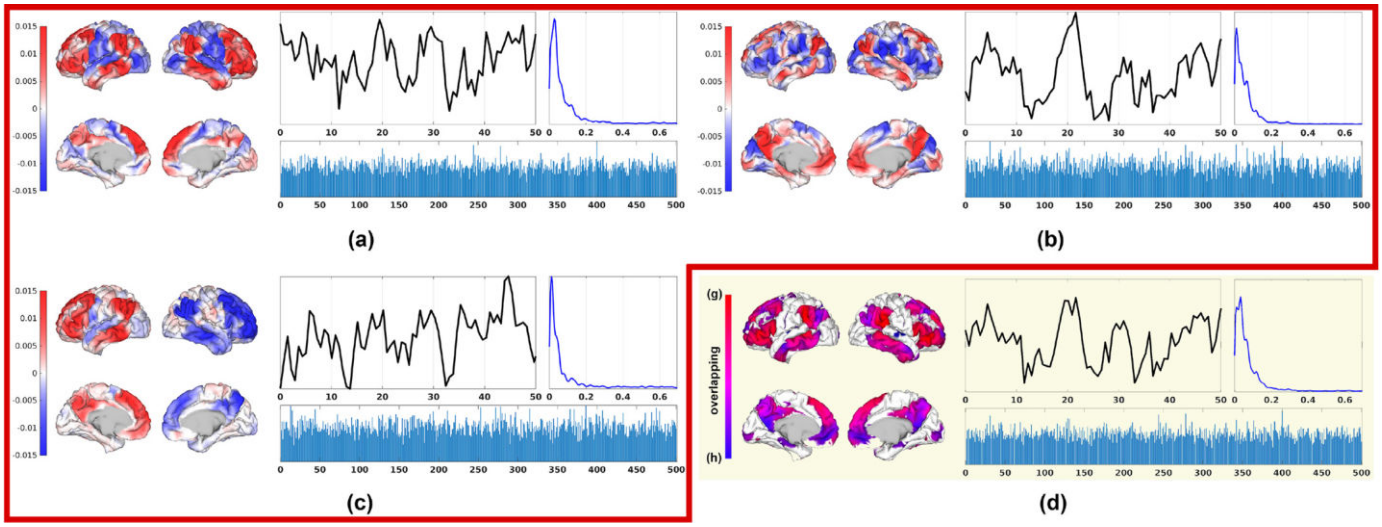

Fig. 3. Subset of the twenty-three identified brain networks that belongs to the default mode category. Red (a) – (c): Three sub-networks of the default mode network; (d) The combined network from (a) and (b), where (a) is encoded in red, (b) is encoded in blue, and purple indicates overlapped regions. In each network, the spatial map is shown on the left with a bipolar color scheme where red represents coherent and blue anti-coherent regions; temporal variations (in secs) are shown on the top middle, where the time series is truncated to 50 s for visual clarity; the subject participation level for 500 subjects in the first session first group is shown on the bottom; the Welch-estimated power spectra (in Hz) of the temporal mode are shown top-right. The peak frequencies are listed in Table S1 in the Supplementary Information.

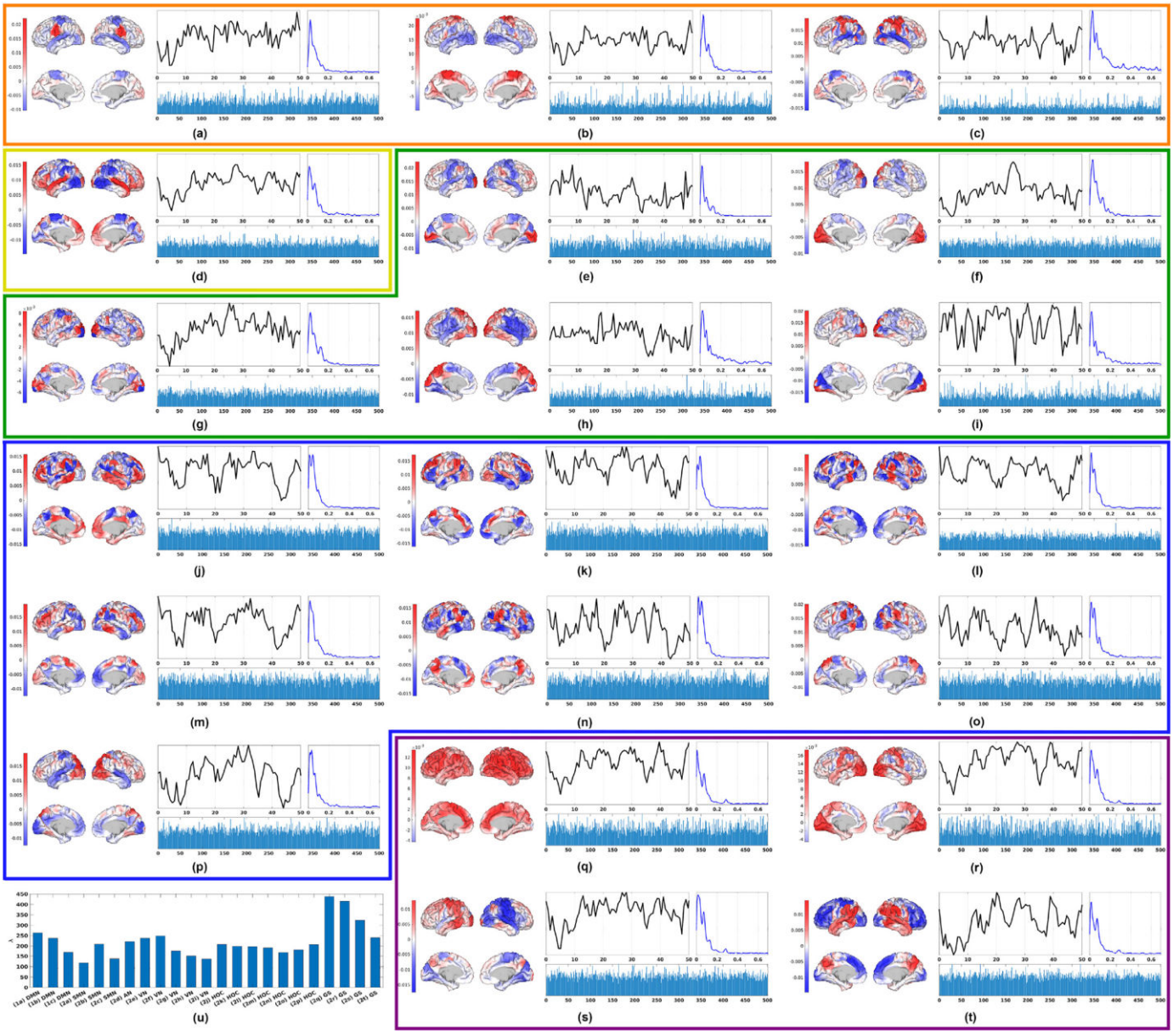

Fig. 4. Twenty of the twenty-three identified brain networks grouped by their functional categories. Orange (a) – (c): somatomotor networks; Yellow (d): auditory network; Green (e) – (i): visual networks; Blue (j) – (p): higher-order cognitive networks; Purple (q) – (t): global signals. See Fig. 3 for the three DMN networks and description of components shown for each network. (u) Plot of the λ values for each network in Figs. 3 and 4 representing the relative degree of activity in each network averaged across the population. Individual strength of participation in each network is found by scaling of λ by the subject participation level.

foot areas, respectively, while network (c) was centered on the hand region, premotor, supplementary motor, and sensory cortices. These somatomotor networks (SMN) show strong coherence in their spectra with a common peak frequency at 0.027 Hz, Fig. 5(c). Across subjects, the large discrepancy in subject participation suggests that there was a subset of participants who were either more active physically during the rs-fMRI sessions or more aware of their bodies and actively focused on keeping still. However, this cross-subject discrepancy was very consistent among the three networks, Fig. 5(d).

One network, Fig. 4(d), was centered on primary auditory cortices (AN), including Heschl's gyrus and the surrounding regions of the superior temporal gyrus. This network was distinct from the remaining 22 networks in the spatial mode. However, the AN is correlated with multiple other networks in the other three modes, Fig. 5.

Five networks, Fig. 4(e) – (i), were centered on visual cortices (VN). Network (e) was centered on the primary visual cortices (striate cortices) along the calcarine fissure (V1, Brodmann's area [BA] 17), while network (f) included V1 as well as secondary and tertiary areas in the cuneus and lingual gyri (V2, V3 and VP, BA 18 and 19). Network (g) included secondary and tertiary areas in cuneus, lingual and lateral occipital gyri as well as the TPJ. Networks (h) and (i) were centered in the visual association areas and showed a strong correspondence, spatially, to the dorsal and ventral visual pathways, respectively. Temporally and spectrally, Fig. 5(b), (c), these five networks appeared to segregate further into three smaller clusters (e, f/g, h/i), suggesting that spatiotemporal interactions across the primary, secondary/tertiary, and visual association networks differ.

Seven networks (Fig. 4(j) – (p)) were centered on higher-order association cortices in the frontal, temporal, and parietal lobes (HOC). Networks (j) and (m) had nodes in the lateral prefrontal cortex, IPL, and inferior temporal lobe, which are well aligned with the central executive control network. Core regions of the network (k), (l), and (n)

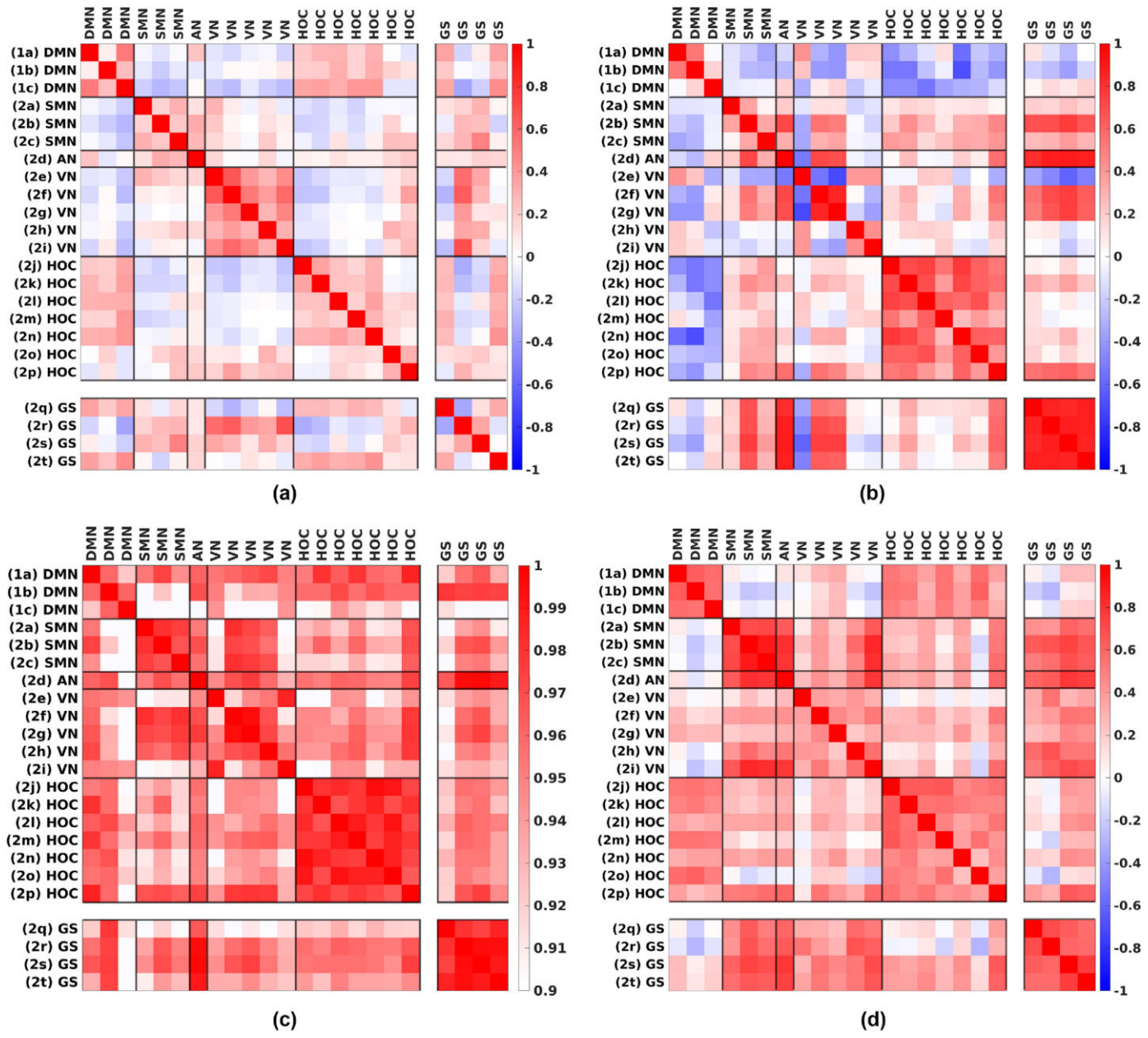

Fig. 5. Cross-correlation matrices of the twenty-three networks. (a) spatial correlation; (b) temporal correlation; (c) spectral correlation; (d) subject correlation. The labels on the axes indicate the functional category each network belongs to: DMN – default mode network; SMN – somatomotor network; AN – auditory network; VN – visual network; HOC – higher-order cognitive network; GS – global signal. The indices inside the parentheses correspond to the sub-figure indices in Figs. 3 and 4. The color bar on the right shows the range of correlation values in each individual matrix.

included anterior midcingulate cortex, bilateral anterior insula, IPL, and TPJ. These three networks correspond to the cingulo-opercular, salience, and ventral attentional network, respectively, and may collectively represent the large-scale midcingulo-insular system (Uddin et al., 2019). Networks (o) and (p) were centered on the superior parietal lobule extending posteriorly along the intraparietal sulcus into the lateral occipital cortex, including areas V3A and the middle temporal complex (MT+), while network (o) also includes prefrontal regions in the vicinity of the frontal eye fields and inferior frontal junction. Together these two networks are close to the canonical dorsal attentional network. In fact, these two networks were spatially segregated from the other HOC networks, Fig. 5(a). However, all HOC networks were highly correlated in their temporal, spectral, and subject modes, Fig. 5(b) – (d). In particular, they showed strong consistency in bi-modal operating frequencies with the lower at 0.011/0.016 Hz and the higher at ~0.04 Hz, Table S1.

In contrast to the above, the final four "networks," Fig. 4(q) – (t), appear to collectively represent the global signals (GS) present in the rs-fMRI data. The Pearson correlations between the four components and the empirically computed global signal are 0.98, 0.90, 0.81, and 0.87 for (q) – (t), respectively. The component (r) has the highest activity level (λ) among all networks, Fig. 4(u). They each exhibit variable spatial patterns with emphasis on different regions of the brain. We observed a very high concordance among the four components in time, spectrum, and the subject mode, Fig. 5(b) – (d). Interestingly, in their spectra, a consistent, unique third peak was shown at 0.288 Hz, which is substantially higher than the peak frequencies of all other networks

and corresponded to a respiration rate of approximately 17 breaths per minute.

3.3. Intrinsic brain networks are spatially overlapped and temporally correlated

The interactions and relations among networks persist in multi-dimensional facets, including space, time, spectrum, and the subject participation level. Moreover, the inter-network relationship spans a hierarchical organizing structure: Networks within a classical functional category (intra-category) have their unique means of interaction, as discussed in the previous section and shown in the six diagonal blocks of Fig. 5. At the same time, networks in one functional category have consistent but differing relations, also in a multi-dimensional manner, to networks in other categories (inter-category), as seen in the off-diagonal blocks in Fig. 5. Of the many inter-categorical relations, the most evident one is the strong and consistent temporal anti-correlations between the DMN and the HOC, Fig. 5(b). This anti-correlation between "task-positive" networks and the DMN, which is also called the "task-negative" network historically, has been widely reported in the literature (Buckner et al., 2008; Buckner and DiNicola, 2019; Raichle, 2015; Raichle and Snyder, 2007). Further, the spatial distribution of networks involved in early developed regions, such as SMN, VN, AN, tend to be anti-correlated to that involved in later developed HOC and DMN, Fig. 5(a). Similar segregation can be observed in the subject mode, where subjects who have higher participation levels in the DMN also have higher participation levels in HOC, but lower in SMN, AN, and VN, while interestingly, the GS components have consistent behavior with the latter, Fig. 5(d). Finally, regardless of positive and negative correlations in space, time, and the subject mode, all networks were operating in similar frequencies, with higher consistency within each functional category and lower between categories, Fig. 5(c) and Table S1.

To better illustrate how these networks interact with each other, we mapped the spatiotemporal patterns of the two sub-networks of the DMN, Fig. 3(a) and (b), onto a common tessellated surface. They were then color-coded and played back in real-time as a video shown in Supplementary Movie S1 (This is similar to Fig. 3(d) but now in a time-evolving manner).

As a comparison, we also identified 23 networks using sICA, as shown in Fig. S5. At the group level, large-scale "more independent" networks, such as SMNs and VNs, are quite similar between NASCAR and ICA. However, for complex networks where multiple regions are involved and perhaps correlated, they are different from each other. These complex networks identified by ICA tend to have lower inter-session/group consistency as compared to their counterparts identified by NASCAR, as shown in Fig. S6. Further, regarding the correlation structures among these networks, the spatial correlation matrix shown in Fig. S7 (a) is an identity matrix, which is expected as spatial ICA imposes independence constraints on the spatial maps. Clusters of networks are present in the temporal and spectral correlation matrices, Fig. S7 (b) and (c), but the patterns appear less clear than those in the NASCAR results. Further, as with other 2D methods, group ICA does not directly produce the third dimension capturing the subject participation level, which is present in the 3D NASCAR model.

3.4. Estimation of subject participation levels embeds the intrinsic properties of brain networks

Figure 6(b) shows the scatter plot between the ADHD index predicted from the held-out data and the measured ADHD index. The Pearson correlation between these two measures is 0.46 with a p-value of 1.42×10^{-12}. A repeated analysis using robust regression method on all data points without exclusion of any outliers showed that this linear relationship is very reliable, where the Pearson correlation between the regression coefficients using the Cook's method and that using a robust linear regression method is 0.96.

Figure 6(c) shows the 10-fold cross-validated classification result as a binary confusion matrix. We are able to achieve 73.3% classification accuracy with a balanced 70.1% specificity and 62.1% sensitivity. In contrast, using the same Peking University dataset, the best performance obtained in the ADHD-200 competition across all teams was 51.1% (The ADHD-200 Consortium, 2012). It also substantially outperforms more recent neural-network-based studies using rs-fMRI data only (Riaz et al., 2020; Zhang et al., 2020) and using a combination of rs-fMRI and structural scans (Zou et al., 2017), where the highest reported accuracy was 65.2% (Zhang et al., 2020).

Figure 6(d) shows the medians and standard errors of the estimated subjects' participation levels across six categories. Consistent with the literature, ADHD subjects present a decreased activity level compared to NT in DMN (Uddin et al., 2008) as well as networks related to cognitive functions (Castellanos and Aoki, 2016). On the other hand, VN, AN, and SMN show an increased level of activity (Cortese et al., 2012) in ADHD subjects relative to NT. This is expected as ADHD subjects tend to be more inattentive and physically hyperactive than NT. We do not see a significant difference in the global components between the two. These group differences are also consistent with that in our preliminary study (Li et al., 2020b). However, in the previous experiment, brain network identification was directly performed on the small ADHD dataset without the use of the functional atlas, hence many networks, such as AN, GS, were not identified.

Figure 7 shows the ADHD index prediction results as well as the binary classification results using networks estimated by group sICA (a, d), PCA (b, e), and the Yeo-17 parcellated atlas (c, f). NASCAR yields better performance in both experiments in comparison to the other three methods, indicating that networks identified from NASCAR may better represent some intrinsic properties of the brain.

When using subject-specific functional connectivity from ICA-dual regression time series as the features, the ADHD index prediction performance resulted in Pearson correlations of 0.24 with ridge regression and 0.17 with lasso regression. This drop relative to use of the network-energy features in Fig. 7 is possibly because the functional connectivity estimates (sample correlations) are noisy given the short fMRI recordings in the ADHD data, and thus do not provide an informative feature set for the prediction task.

Table 1 shows the prediction results for the three IQ measures using networks identified from NASCAR, group sICA, PCA, and the Yeo-17 atlas as measured by Pearson correlation between the predicted and measured IQ. The corresponding scatter plots are shown in Fig. S8. Interestingly, the subject participation levels estimated from the rs-fMRI data could better predict Crystallized IQ than Fluid IQ, regardless of the underlying methods used for network identification. In comparison across different methods, NASCAR consistently outperforms the other three in predicting all three IQ measures as reflected by the Pearson correlation measures, again indicating that networks identified by NASCAR may better reflect the complex functional organization of the human brain.

4. Discussion

The present study informs our understanding of the intrinsic spatiotemporal organization of the human connectome by describing a functional atlas consisting of a set of twenty-three resting-state networks with associated spatial and temporal maps. Critically, these networks were derived without the imposition of mathematical constraints, while demonstrating high reproducibility across four large, independent groups/sessions. Furthermore, these networks are largely symmetric at the macro-scale but asymmetric at the meso-scale. This is particularly encouraging because any symmetry that does arise comes directly from the data rather than the underlying algorithmic approach. In addition, the spatial topography of these multi-dimensional networks resembled many of the canonical resting-state networks (RSNs), including the DMN (Buckner et al., 2008; Buckner and DiNicola, 2019; Raichle, 2015;

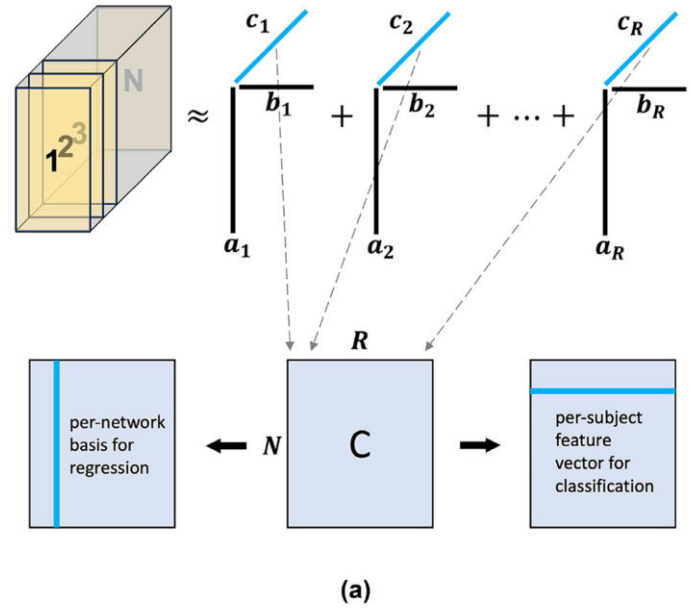

(a)

	Predicted ADHD	Predicted NT
ADHD	54	33
NT	23	100

Specificity = 70.1% Sensitivity = 62.1% Accuracy = 73.3%

(c)

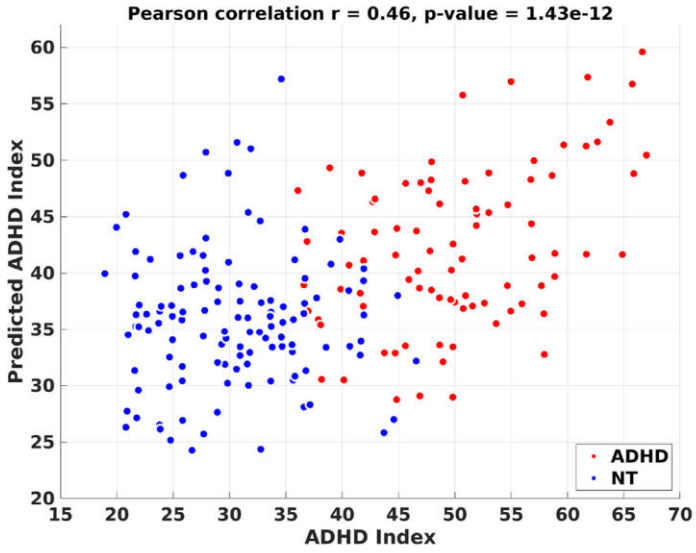

(b)

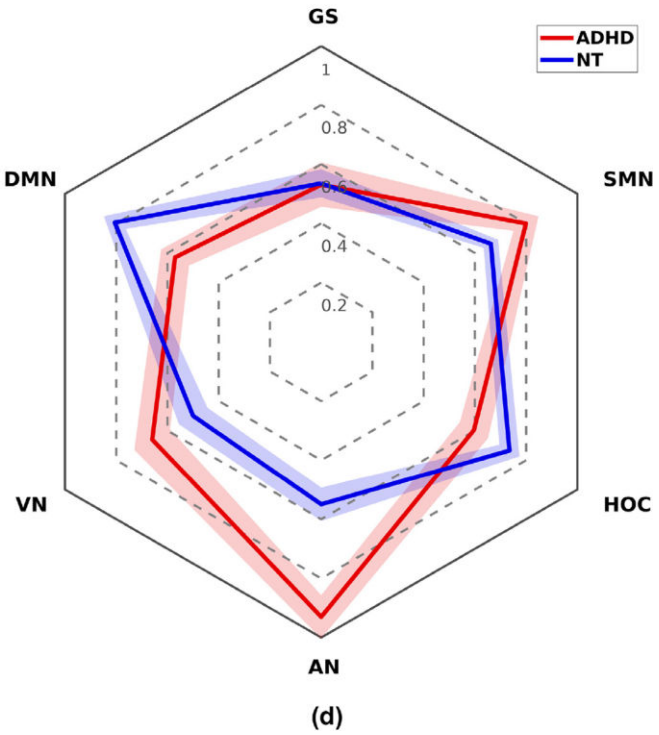

(d)

Fig. 6. Results of applications of functional network atlas to the ADHD dataset. (a) The feature matrix C is formed by concatenation of the estimated subject participation scores. It could be used as per-network bases for a regression study (left arrow) or per-subject feature vectors for classification tasks (right arrow); (b) Scatter plot between the predicted ADHD index (y-axis) and the measured ADHD index (x-axis). Red dots mark the ADHD subjects, and the blue dots mark the neurotypical (NT) subjects; (c) Binary confusion matrix of the classification result, with accuracy, specificity, and sensitivity reported below the table; (d) Radar plot of the normalized median subject participation level in six network categories for ADHD in red and NT in blue. The shaded areas represent their corresponding standard errors.

Table 1
Prediction of IQ scores.

Pearson Correlation (p-value)	Fluid IQ	Crystallized IQ	Total IQ
NASCAR	0.27 (3.4×10^{-9})	0.32 (6.8×10^{-13})	0.30 (3.0×10^{-11})
ICA	0.21 (2.6×10^{-6})	0.28 (6.6×10^{-10})	0.24 (6.2×10^{-8})
PCA	0.13 (3.6×10^{-3})	0.29 (5.5×10^{-11})	0.26 (7.5×10^{-9})
Parcellation	0.16 (3.4×10^{-4})	0.27 (4.0×10^{-9})	0.23 (7.8×10^{-7})

Raichle and Snyder, 2007), the visual networks, and the higher-order cognitive networks (Uddin et al., 2019).

A unique property of the tensor-based NASCAR method is that it intrinsically includes an extra (third) dimension that encodes rs-fMRI information for each subject. In contrast, group-ICA and related methods typically concatenate the time series at each location for all subjects into a single dimension to create a matrix. While it is possible to compute a per-subject participation value once ICA networks are found, these methods do not exploit any *intrinsic* low-rank structure embedded directly in the third-order tensor. In fact, it is this embedding into

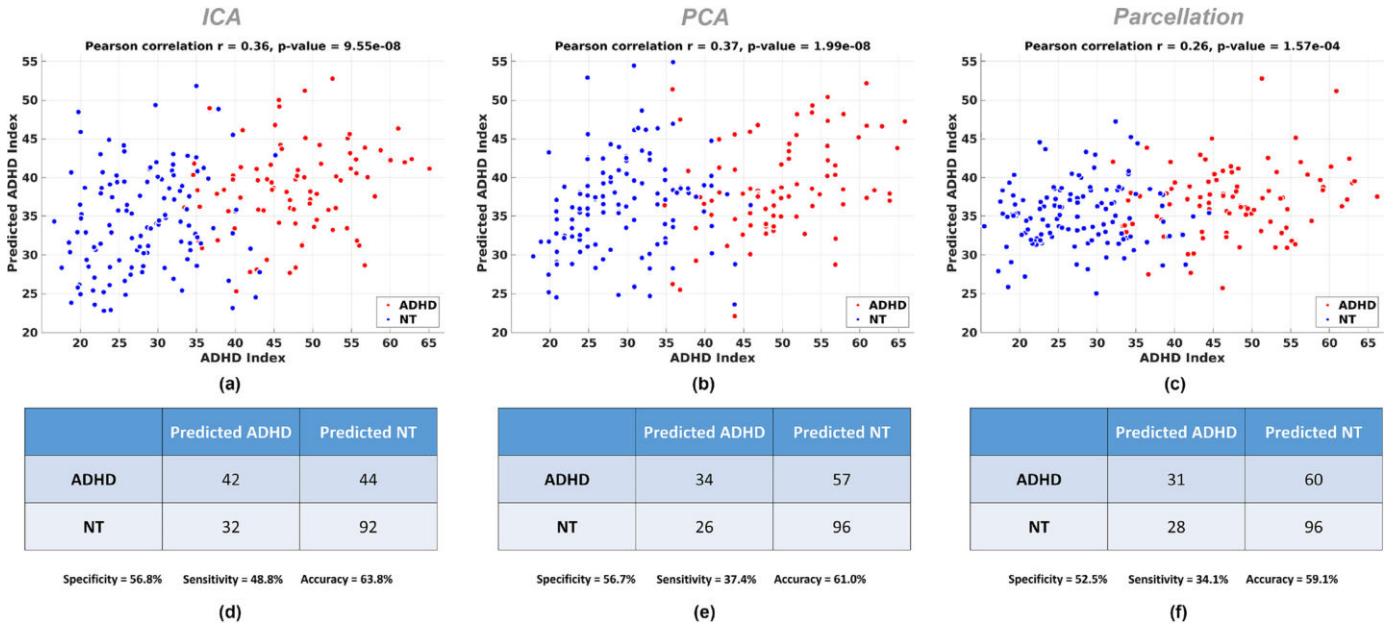

	Predicted ADHD	Predicted NT
ADHD	42	44
NT	32	92

Specificity = 56.8% Sensitivity = 48.8% Accuracy = 63.8%

(d)

	Predicted ADHD	Predicted NT
ADHD	34	57
NT	26	96

Specificity = 56.7% Sensitivity = 37.4% Accuracy = 61.0%

(e)

	Predicted ADHD	Predicted NT
ADHD	31	60
NT	28	96

Specificity = 52.5% Sensitivity = 34.1% Accuracy = 59.1%

(f)

Fig. 7. ADHD index prediction result based on networks identified using other commonly used methods. Scatter plots between the predicted ADHD index (y-axis) and the measured ADHD index (x-axis) are shown in (a) using group sICA; (b) PCA; and (c) Yeo's 17-network parcellation. (d) – (f) show the corresponding confusion matrices for the three methods.

a third-order tensor rather than a matrix to exploit low-rank structure that allows relaxation of the independence assumption required to obtain meaningful decompositions in the matrix case.

In order to achieve this low-rank structure, the time series need to be temporally synchronized across subjects. While this is relatively straightforward for event-related studies, the spontaneous nature of rs-fMRI presents a challenge. Each subject's brain activity is independent. The BrainSync (Akrami et al., 2019; Joshi et al., 2018a) transform can, however, produce temporal-synchronization by exploiting the strong similarities in temporal correlations between brain regions across subjects. Similar to hyper-alignment (Haxby et al., 2011), an orthogonal transform is applied to each subject's fMRI data. However, unlike hyper-alignment, which operates in the spatial domain, BrainSync produces a *temporal alignment or synchronization* at homologous regions. Once this alignment is performed, tensor decomposition allows identification of spatiotemporal networks. It is also worth noting that BrainSync is an orthogonal transform, hence invertible. This orthogonality ensures that the within-subject spatial correlation structure contained in the original data is preserved (Joshi et al., 2018a).

As an indication of the degree to which the NASCAR decomposition can model network activity in rs-fMRI, Fig. S9 shows the cumulative variance explained by principal component analysis (PCA), NASCAR, and sICA. The components from PCA, as expected, provide an upper bound because of the orthogonality property between components, which maximizes variance explained across all possible decompositions at a given rank (Golub and Van Loan, 2013). However, such an orthogonality condition is unlikely to be biologically plausible for brain networks. Compared with components from ICA, NASCAR consistently has a higher cumulative variance explained, even though it has shared (non-orthogonal) modes in both space and time.

The results presented above assign subjects randomly to the two groups of 500 subjects from the HCP database. As a result, twins were not both assigned to the same group. Since there is a relatively large fraction of twins (183 twin pairs [366 subjects] out of 1000 subjects), this may impact the independence assumption between the two groups. To investigate this effect, we re-sorted the data and assigned each pair of twins to a single group. We then recomputed the NASCAR decomposition. Correlations between the networks identified using these two different allocations of twins is shown in Fig. S10. Visually these networks appear very similar and based on the correlation values, we believe the two sortings of the data would produce essentially indistinguishable results to those presented in Figs. 3–5.

We observed three multi-dimensional RSNs related to the DMN (Fig. 3). Two of these, Fig. 3(a) and (b), were bilaterally symmetric and, when combined, resembled the canonical DMN, Fig. 3(d), suggesting that individually they represent subsystems of the DMN. Prior studies have demonstrated that the DMN can be decomposed into at least two partially-distinct subsystems that are inter-connected to and interact with each other (Buckner et al., 2008; Buckner and DiNicola, 2019). Using a hierarchical clustering approach, these have been described as a "dorsal medial subsystem" and a "medial temporal subsystem" (Andrews-Hanna et al., 2014, 2010; Buckner and DiNicola, 2019), as shown in Fig. S11 (a). The spatial topography of Fig. 3(a) and (b) strongly resemble these two subsystems. Also, the parcellation scheme from Yeo and his colleagues (Yeo et al., 2011) revealed three DMN parcels, the ensemble of which is substantially consistent with both our findings and those of Andrews-Hanna, Fig. S11 (b). Recently, a similar topography of the two subsystems has also been shown by Harrison and his colleagues using a Bayesian approach (Harrison et al., 2020), referred to as the canonical DMN and a variate of the DMN, Fig. S11 (c). The overall configurations of the two subsystems using the NASCAR method are also strongly consistent with the spatial maps obtained using seeded correlation as shown in Fig. S11 (d) with global signal regression (GSR) and (e) without GSR. Following (Andrews-Hanna et al., 2014, 2010), in these maps a seed was placed in the TPL for the dorsal medial subsystem with a second seed in the posterior inferior parietal lobule (pIPL) for the medial temporal subsystem. The NASCAR maps in Fig. 3(a) and (b) exhibit more distinct functional boundaries than the seeded correlation maps. Further, some negatively correlated regions, such as the ventral posterior cingulate cortex (vPCC) and the ventromedial prefrontal cortex (vmPFC), are missing in the seeded correlation maps due to the overlapping of the two subsystems. We measured the consistency between the NASCAR maps and corresponding seeded correlation maps separately for each of the two subsystems using Pearson

Table 2
Consistency between DMN subsystem spatial maps obtained using NASCAR/ICA and those obtained using the seeded correlation method. GSR – Global signal regression.

Pearson Correlation	NASCAR w/ GSR	ICA w/ GSR	NASCAR w/o GSR	ICA w/ GSR
Dorsal Medial Subsystem	0.75	0.52	0.71	0.57
Medial Temporal Subsystem	0.76	0.39	0.68	0.37

correlations. We also repeated this measure for the ICA maps. Results shown in Table 2 indicate that the NASCAR maps have higher consistency with the seeded correlation results than the ICA-based results for both subsystems regardless of whether GSR is applied or not. Furthermore, our results show that the two subsystems have different spectral characteristics, with the dorsal medial subsystem demonstrating peak power at a higher frequency than the medial temporal subsystem. In fact, a prior study utilizing repetitive transcranial magnetic stimulation (rTMS) and fMRI demonstrated that two different frequencies of rTMS applied to the same DMN node in the pIPL induced two topographically distinct changes in functional connectivity (Eldaief et al., 2011). Rather than a single node possessing multiple, functionally distinct relationships among its distributed partners, our results suggest that a single node may belong to two or more spatiotemporal networks that are superimposed on top of each other, as illustrated in Movie S1.

In addition to the two networks described above, our results revealed a third default mode-related network, Fig. 3(c). The spatial topography of this network was nearly identical to Fig. 3(a) and (b). But spatiotemporally, there were strong correlations across the hubs within hemisphere and anti-correlations between hemispheres, which may reflect left-right asymmetries in the activity within the DMN. A similar component is also found when using the group ICA method (Fig. S5 (c)), but with a substantially lower consistency across sessions compared to other stable ICA networks, Fig. S6. To our knowledge, this left-right asymmetric DMN component has not been reported in other rs-fMRI studies. However, this is consistent with the temporal variations of the DMN, as demonstrated by magnetoencephalography (MEG) (de Pasquale et al., 2010).

Overall, these new observations about the spatiotemporal relationship between the two sub-networks could potentially provide a deeper insight into the functional organization of the human DMN as well as how alterations in the spatiotemporal dynamics between these subsystems might contribute to cognitive dysfunction (Andrews-Hanna et al., 2014; Kim, 2012; Silbersweig, 2013).

In the canonical 7-network RSN parcellation (Yeo et al., 2011), the somatomotor network is a single network, while at least two other subsystems have also been observed, including right, left (Smith et al., 2009), dorsal, and ventral (face) subsystems (Gordon et al., 2016; Yeo et al., 2011). Spatially, our results are similar to the higher-order parcellation schemes. They further demonstrate modest correlations in space and time, Fig. 5(a) (b), but strong coherence in their spectra with a common peak frequency at 0.027 Hz, which, in turn, is readily dissociable from the spectral characteristics of the auditory network.

Five networks included core components of the visual system. Prior studies have demonstrated various occipital networks, including medial and lateral networks, and one corresponding to the occipital pole. However, to our knowledge, this is the first study to identify RSNs corresponding to the dorsal ("where") and ventral ("what") visual pathways first proposed 40+ years ago on the basis of neuropsychological, electrophysiological, behavioral evidence (Goodale and Milner, 1992; Mishkin et al., 1983), and later, structural connectivity (Catani, 2003). Furthermore, our results demonstrate unique spectral characteristics across the visual networks. First, there is a peak at 0.06 Hz which is unique to the visual networks and was not observed across any other networks. Additionally, the networks corresponding to the primary visual (e) and auditory (d) exhibited peak power at the same frequency (0.016 Hz). Again, these findings suggest that elucidating the spectral characteristics of the RSNs may be key to understanding how information is represented or transmitted across the human brain.

Seven networks were centered on higher-order association cortices in the frontal, temporal, and parietal lobes. The spectral characteristics of these networks suggest that while the HOC networks represent different subsystems, they operate at and, therefore, may interact at specific frequencies. Furthermore, while the higher frequency (~0.04 Hz) is unique to the HOC, the lower frequencies were shared with other networks, including subsystems within the DMN, auditory and visual networks, suggesting a mechanism by which the attentional and executive subsystems may influence information processing across other subsystems.

The four global components, Fig. 4 (q, r, s, t), exhibit strong correlations with the global signal computed from the rs-fMRI data empirically, which is often used in global signal regression. These global signals can partly be attributed to vascular effects or neurovascular coupling caused by respiratory and/or cardiac activity (Birn et al., 2006; Chang et al., 2009; Logothetis and Wandell, 2004). In particular, Fig. 4(r) and (t) show very similar spatial maps to the "physiological network" (the red and blue "networks", respectively) reported previously (Chen et al., 2020), which is obtained directly using linear regression on physiological recordings. In contrast, NASCAR identified these four global signals in a purely data-driven manner without access to physiological measures. Frequency-wise, all four components exhibit a unique peak at ~0.288 Hz, which is substantially higher than other networks. It is also aligned with the frequency of respiration (~17 breaths per minute). We note that this peak frequency is specific to the subject we chose for the inverse BrainSync temporal transformation, and we observed inconsistent peak frequencies among the subjects. This is because different subjects may have different respiratory/cardiac rates, which are the main sources of the global signals. Further, it has been shown that physiological components cannot be fully removed from rs-fMRI data due to their spatial heterogeneity (Chang et al., 2009; Chen et al., 2020). In fact, the four components identified in this work depict distinct spatial patterns, which are also partially overlapped with each other. There has been a long debate on whether global signal regression (GSR) should be applied to fMRI data (Murphy and Fox, 2017). Instead of heuristically regressing out a single time course (the global signal), NASCAR is capable of modeling these spatially heterogeneous components as low-rank factors, hence perhaps providing an improved approach to decoupling neuronal brain networks from physiological components. To demonstrate the changes with/without GSR. We reran NASCAR after GSR on each subject. Fig. S12 shows the spatial (left) and temporal (right) correlation between the networks found by NASCAR with and without GSR. The four global signals were highly suppressed after GSR, while other "non-physiological" networks are highly reproducible with most correlations > 0.8, which makes them visually difficult to distinguish. One exception is the temporal mode for the auditory network, which is – interestingly – likely highly correlated with the global signal thus impacted by the GSR.

By generating these highly reproducible, spatially overlapped, and temporally correlated brain networks, we have constructed a "functional network atlas", representing the functional spatiotemporal organization of the human brain common across the healthy population. This atlas can be used to study group differences in brain networks and is *particularly powerful for studies with a limited number of subjects/patients*. Us-

ing this functional network atlas, one could obtain a reliable estimation of brain network properties by a least-square fitting of individual subject's rs-fMRI data to the functional atlas, which could be difficult if the analysis is done directly on the small dataset. As we demonstrated in the ADHD study, the estimated subject mode not only provides individual network information for classification and prediction of ADHD indices, but also allows us to investigate differences in brain activity between ADHD subjects and controls in a variety of brain networks concurrently, hence potentially facilitating the exploration of neurological differences associated with ADHD. Applications of the procedure used in the ADHD study to other neurological and psychological conditions could be promising future directions.

We hypothesize that the brain networks identified by NASCAR from resting state data are intrinsic to the brain, with or without task present. Indeed, we observed many of them in decomposing the HCP language task fMRI data in our previous work, such as the DMN, VN, SMN, AN, and several HOCs (Li et al., 2021). However, NASCAR is a data-driven approach seeking components that explain most of the variance in the data. Therefore, when applied to task fMRI, task-related components may dominate. The brain's response to a task may involve activity over multiple networks that cannot be temporally resolved given the slow hemodynamic response intrinsic to fMRI. As a result, there may be discordance between networks identified from task and resting state fMRI. Exploration of the relationship between identified and intrinsic networks in task vs. resting state data (Di et al., 2013; Kraus et al., 2021) is a current topic of considerable interest to which the NASCAR approach could contribute in future studies.

In this study, we used a maximum rank of 50 in the NASCAR decomposition. Selection of the maximum bound for the rank is a common issue for all blind source separate methods in application to fMRI data. Many groups have reported that 50 should be sufficient (Biswal et al., 2010; Calhoun et al., 2001; Harrison et al., 2020). In our experiments, we examined the results for ranks 20, 30, and 40 and compared them with the results for rank 50. We found that 30 is insufficient to identify all reproducible networks (the last reproducible network was identified at rank 32). All 23 reproducible networks were found in the rank 40 decomposition and were highly consistent with rank 50 results due to the stability of the NASCAR algorithm, which increases the model rank by one at each stage, using the previous lower-rank solution for initialization (Li et al., 2021).

One of the limitations of the NASCAR pipeline is that it requires accurate spatial inter-subject coregistration in addition to the temporal synchronization. The low-rank model will fail if there is substantial spatial misalignment between subjects, although importantly, the same concern arises with group-ICA and related decompositions. The combination of BrainSync with some more advanced spatial coregistration approaches (Balakrishnan et al., 2019; Robinson et al., 2014; Yeo et al., 2010) could be beneficial for further improvement of the network identification results. A second potential limitation is that BrainSync will perfectly align time series only to the degree that the underlying temporal-correlation structure is common among subjects. The differences among subjects after alignment reflect underlying differences in this correlation. However, since we use an unbiased group-based approach in the BrainSync transform (Akrami et al., 2019) to find the best match across all subjects, these differences can be viewed as informative indicators of the way in which each individual differs from the group. It is these differences that are encoded in the subject participation scores used in the ADHD study.

In this work, we identified a set of common brain networks from a large set of healthy subjects' fMRI data using a low-rank tensor (canonical polyadic) model. However, we did not model or estimate individual networks at the subject level. Similar to the dual regression strategy employed in the group ICA method, one can obtain estimates of individual spatial/temporal modes using a least square fit to the group results in the other mode. Exploration of these individualized maps and how they correlate with neurological and psychological measures could also be a promising future direction.

Declaration of competing interest

The authors declare no competing interests.

Credit authorship contribution statement

Jian Li: Conceptualization, Methodology, Investigation, Formal analysis, Validation, Software, Writing – original draft, Writing – review & editing, Visualization. **Yijun Liu:** Investigation, Formal analysis, Validation, Writing – review & editing, Visualization. **Jessica L. Wisnowski:** Investigation, Validation, Writing – review & editing, Supervision, Funding acquisition. **Richard M. Leahy:** Conceptualization, Methodology, Investigation, Validation, Resources, Writing – review & editing, Supervision, Funding acquisition.

Data availability

The data used in this study are publicly available from the Human Connectome Project, Young Adult Study (https://www.humanconnectome.org/study/hcp-young-adult) and the International Neuroimaging Data-Sharing Initiative ADHD-200 dataset (https://fcon_1000.projects.nitrc.org/indi/adhd200).

For research purposes, we release the multi-dimensional functional atlas via Figshare (https://doi.org/10.6084/m9.figshare.c.5739128) and the open-access code is released at the GitHub repository (https://neuroimageusc.github.io/main)

Acknowledgement

This work was supported by National Institutes of Health grants R01-NS074980, R01-EB026299, R01-NS089212, and K23-HD099309.

Supplementary materials

Supplementary material associated with this article can be found, in the online version, at doi:10.1016/j.neuroimage.2023.119944.

References

Akrami, H., Joshi, A.A., Li, J., Leahy, R.M., 2019. Group-wise alignment of resting fMRI in space and time. In: Angelini, E.D., Landman, B.A. (Eds.), SPIE Medical Imaging 2019: Image Processing. Presented at the Image Processing, San Diego, United States, p. 103. doi:10.1117/12.2512564.

Allen, E.A., Damaraju, E., Plis, S.M., Erhardt, E.B., Eichele, T., Calhoun, V.D., 2014. Tracking whole-brain connectivity dynamics in the resting state. Cerebral Cortex 24, 663–676. doi:10.1093/cercor/bhs352.

Andrews-Hanna, J.R., Reidler, J.S., Sepulcre, J., Poulin, R., Buckner, R.L., 2010. Functional-anatomic fractionation of the brain's default network. Neuron 65, 550–562. doi:10.1016/j.neuron.2010.02.005.

Andrews-Hanna, J.R., Smallwood, J., Spreng, R.N., 2014. The default network and self-generated thought: component processes, dynamic control, and clinical relevance: the brain's default network. Ann. N.Y. Acad. Sci. 1316, 29–52. doi:10.1111/nyas.12360.

Balakrishnan, G., Zhao, A., Sabuncu, M.R., Guttag, J., Dalca, A.V., 2019. VoxelMorph: a learning framework for deformable medical image registration. IEEE Trans. Med. Imaging 38, 1788–1800. doi:10.1109/TMI.2019.2897538.

Birn, R.M., Diamond, J.B., Smith, M.A., Bandettini, P.A., 2006. Separating respiratory-variation-related fluctuations from neuronal-activity-related fluctuations in fMRI. Neuroimage 31, 1536–1548. doi:10.1016/j.neuroimage.2006.02.048.

Biswal, B.B., Mennes, M., Zuo, X.-N., Gohel, S., Kelly, C., Smith, S.M., Beckmann, C.F., Adelstein, J.S., Buckner, R.L., Colcombe, S., Dogonowski, A.-M., Ernst, M., Fair, D., Hampson, M., Hoptman, M.J., Hyde, J.S., Kiviniemi, V.J., Kotter, R., Li, S.-J., Lin, C.-P., Lowe, M.J., Mackay, C., Madden, D.J., Madsen, K.H., Margulies, D.S., Mayberg, H.S., McMahon, K., Monk, C.S., Mostofsky, S.H., Nagel, B.J., Pekar, J.J., Peltier, S.J., Petersen, S.E., Riedl, V., Rombouts, S.A.R.B., Rypma, B., Schlaggar, B.L., Schmidt, S., Seidler, R.D., Siegle, G.J., Sorg, C., Teng, G.-J., Veijola, J., Villringer, A., Walter, M., Wang, L., Weng, X.-C., Whitfield-Gabrieli, S., Williamson, P., Windischberger, C., Zang, Y.-F., Zhang, H.-Y., Castellanos, F.X., Milham, M.P., 2010. Toward discovery science of human brain function. Proc. Natl. Acad. Sci. 107, 4734–4739. doi:10.1073/pnas.0911855107.

Bressler, S.L., Menon, V., 2010. Large-scale brain networks in cognition: emerging methods and principles. Trends Cogn. Sci. (Regul. Ed.) 14, 277–290. doi:10.1016/j.tics.2010.04.004.

Buckner, R.L., Andrews-Hanna, J.R., Schacter, D.L., 2008. The brain's default network: anatomy, function, and relevance to disease. Ann. N. Y. Acad. Sci. 1124, 1–38. doi:10.1196/annals.1440.011.

Buckner, R.L., DiNicola, L.M., 2019. The brain's default network: updated anatomy, physiology and evolving insights. Nat. Rev. Neurosci. 20, 593–608. doi:10.1038/s41583-019-0212-7.

Calhoun, V.D., Adali, T., Pearlson, G.D., Pekar, J.J., 2001. A method for making group inferences from functional MRI data using independent component analysis. Hum. Brain Mapp. 14, 140–151. doi:10.1002/hbm.1048.

Calhoun, V.D., Liu, J., Adalı, T., 2009. A review of group ICA for fMRI data and ICA for joint inference of imaging, genetic, and ERP data. Neuroimage 45, S163–S172. doi:10.1016/j.neuroimage.2008.10.057.

Castellanos, F.X., Aoki, Y., 2016. Intrinsic functional connectivity in attention-deficit/hyperactivity disorder: a science in development. Biol. Psychiatry: Cognit. Neurosci. Neuroimag. 1, 253–261. doi:10.1016/j.bpsc.2016.03.004.

Catani, M., 2003. Occipito-temporal connections in the human brain. Brain 126, 2093–2107. doi:10.1093/brain/awg203.

Chang, C., Cunningham, J.P., Glover, G.H., 2009. Influence of heart rate on the BOLD signal: the cardiac response function. Neuroimage 44, 857–869. doi:10.1016/j.neuroimage.2008.09.029.

Chen, J.E., Lewis, L.D., Chang, C., Tian, Q., Fultz, N.E., Ohringer, N.A., Rosen, B.R., Polimeni, J.R., 2020. Resting-state "physiological networks. Neuroimage 213, 116707. doi:10.1016/j.neuroimage.2020.116707.

Cortes, C., Vapnik, V., 1995. Support-vector networks. Mach Learn 20, 273–297. doi:10.1007/BF00994018.

Cortese, S., Kelly, C., Chabernaud, C., Proal, E., Di Martino, A., Milham, M.P., Castellanos, F.X., 2012. Toward systems neuroscience of ADHD: a meta-analysis of 55 fMRI studies. AJP 169, 1038–1055. doi:10.1176/appi.ajp.2012.11101521.

Cox, R.W., 1996. AFNI: software for analysis and visualization of functional magnetic resonance neuroimages. Comput. Biomed. Res. 29, 162–173. doi:10.1006/cbmr.1996.0014.

Craddock, R.C., James, G.A., Holtzheimer, P.E., Hu, X.P., Mayberg, H.S., 2012. A whole brain fMRI atlas generated via spatially constrained spectral clustering. Hum. Brain Mapp 33, 1914–1928. doi:10.1002/hbm.21333.

Dadi, K., Varoquaux, G., Machlouzarides-Shalit, A., Gorgolewski, K.J., Wassermann, D., Thirion, B., Mensch, A., 2020. Fine-grain atlases of functional modes for fMRI analysis. Neuroimage 221, 117126. doi:10.1016/j.neuroimage.2020.117126.

de Pasquale, F., Della Penna, S., Snyder, A.Z., Lewis, C., Mantini, D., Marzetti, L., Belardinelli, P., Ciancetta, L., Pizzella, V., Romani, G.L., Corbetta, M., 2010. Temporal dynamics of spontaneous MEG activity in brain networks. Proc. Natl. Acad. Sci. 107, 6040–6045. doi:10.1073/pnas.0913863107.

Di, X., Gohel, S., Kim, E., Biswal, B., 2013. Task vs. rest - different network configurations between the coactivation and the resting-state brain networks. Front. Hum. Neurosci. 7.

Eldaief, M.C., Halko, M.A., Buckner, R.L., Pascual-Leone, A., 2011. Transcranial magnetic stimulation modulates the brain's intrinsic activity in a frequency-dependent manner. Proc. Natl. Acad. Sci. 108, 21229–21234. doi:10.1073/pnas.1113103109.

Farahibozorg, S.-R., Bijsterbosch, J.D., Gong, W., Jbabdi, S., Smith, S.M., Harrison, S.J., Woolrich, M.W., 2021. Hierarchical modelling of functional brain networks in population and individuals from big fMRI data. Neuroimage 243, 118513. doi:10.1016/j.neuroimage.2021.118513.

Fox, M.D., Raichle, M.E., 2007. Spontaneous fluctuations in brain activity observed with functional magnetic resonance imaging. Nat. Rev. Neurosci. 8, 700–711. doi:10.1038/nrn2201.

Gale, D., Shapley, L.S., 1962. College admissions and the stability of marriage. Am. Math. Month. 69, 9. doi:10.2307/2312726.

Glasser, M.F., Coalson, T.S., Robinson, E.C., Hacker, C.D., Harwell, J., Yacoub, E., Ugurbil, K., Andersson, J., Beckmann, C.F., Jenkinson, M., Smith, S.M., Van Essen, D.C., 2016. A multi-modal parcellation of human cerebral cortex. Nature 536, 171–178. doi:10.1038/nature18933.

Glasser, M.F., Sotiropoulos, S.N., Wilson, J.A., Coalson, T.S., Fischl, B., Andersson, J.L., Xu, J., Jbabdi, S., Webster, M., Polimeni, J.R., Van Essen, D.C., Jenkinson, M., 2013. The minimal preprocessing pipelines for the Human Connectome Project. Neuroimage 80, 105–124. doi:10.1016/j.neuroimage.2013.04.127.

Golub, G.H., Van Loan, C.F., 2013. Matrix computations. Johns Hopkins studies in the Mathematical Sciences, 4th edition. ed The Johns Hopkins University Press, Baltimore.

Goodale, M.A., Milner, A.D., 1992. Separate visual pathways for perception and action. Trends Neurosci. 15, 20–25. doi:10.1016/0166-2236(92)90344-8.

Gordon, E.M., Laumann, T.O., Adeyemo, B., Huckins, J.F., Kelley, W.M., Petersen, S.E., 2016. Generation and evaluation of a cortical area parcellation from resting-state correlations. Cereb. Cortex 26, 288–303. doi:10.1093/cercor/bhu239.

Harris, K.D., Mrsic-Flogel, T.D., 2013. Cortical connectivity and sensory coding. Nature 503, 51–58. doi:10.1038/nature12654.

Harrison, S.J., Bijsterbosch, J.D., Segerdahl, A.R., Fitzgibbon, S.P., Farahibozorg, S.-R., Duff, E.P., Smith, S.M., Woolrich, M.W., 2020. Modelling subject variability in the spatial and temporal characteristics of functional modes. Neuroimage 222, 117226. doi:10.1016/j.neuroimage.2020.117226.

Harrison, S.J., Woolrich, M.W., Robinson, E.C., Glasser, M.F., Beckmann, C.F., Jenkinson, M., Smith, S.M., 2015. Large-scale probabilistic functional modes from resting state fMRI. Neuroimage 109, 217–231. doi:10.1016/j.neuroimage.2015.01.013.

Harshman, R.A., 1970. Foundations of the PARAFAC procedure: models and conditions for an explanatory multimodal factor analysis. UCLA Work. Paper. Phonetic. 16, 1–84.

Haxby, J.V., Guntupalli, J.S., Connolly, A.C., Halchenko, Y.O., Conroy, B.R., Gobbini, M.I., Hanke, M., Ramadge, P.J., 2011. A common, high-dimensional model of the representational space in human ventral temporal cortex. Neuron 72, 404–416. doi:10.1016/j.neuron.2011.08.026.

Hutchison, R.M., Womelsdorf, T., Allen, E.A., Bandettini, P.A., Calhoun, V.D., Corbetta, M., Della Penna, S., Duyn, J.H., Glover, G.H., Gonzalez-Castillo, J., Handwerker, D.A., Keilholz, S., Kiviniemi, V., Leopold, D.A., de Pasquale, F., Sporns, O., Walter, M., Chang, C., 2013. Dynamic functional connectivity: promise, issues, and interpretations. Neuroimage 80, 360–378. doi:10.1016/j.neuroimage.2013.05.079.

Jenkinson, M., Beckmann, C.F., Behrens, T.E.J., Woolrich, M.W., Smith, S.M., 2012. FSL. Neuroimage 782–790. doi:10.1016/j.neuroimage.2011.09.015, 20 YEARS OF fMRI 62.

Joshi, A.A., Chong, M., Li, J., Choi, S., Leahy, R.M., 2018a. Are you thinking what I'm thinking? Synchronization of resting fMRI time-series across subjects. Neuroimage 172, 740–752. doi:10.1016/j.neuroimage.2018.01.058.

Joshi, A.A., McCoy, D., Chong, M., Li, J., Choi, S., Shattuck, D.W., Leahy, R.M., 2018b. BFP: brainSuite fMRI pipeline. 24th Annual Meeting of the Organization for Human Brain Mapping.

Karahanoğlu, F.I., Van De Ville, D., 2015. Transient brain activity disentangles fMRI resting-state dynamics in terms of spatially and temporally overlapping networks. Nat. Commun. 6, 7751. doi:10.1038/ncomms8751.

Kelly, R.E., Alexopoulos, G.S., Wang, Z., Gunning, F.M., Murphy, C.F., Morimoto, S.S., Kanellopoulos, D., Jia, Z., Lim, K.O., Hoptman, M.J., 2010. Visual inspection of independent components: defining a procedure for artifact removal from fMRI data. J. Neurosci. Methods 189, 233–245. doi:10.1016/j.jneumeth.2010.03.028.

Kim, H., 2012. A dual-subsystem model of the brain's default network: self-referential processing, memory retrieval processes, and autobiographical memory retrieval. Neuroimage 61, 966–977. doi:10.1016/j.neuroimage.2012.03.025.

Kraus, B.T., Perez, D., Ladwig, Z., Seitzman, B.A., Dworetsky, A., Petersen, S.E., Gratton, C., 2021. Network variants are similar between task and rest states. Neuroimage 229, 117743. doi:10.1016/j.neuroimage.2021.117743.

Kruskal, J.B., 1989. Rank, decomposition, and uniqueness for 3-way and n-way arrays. In: Multiway Data Analysis. North-Holland Publishing Co., NLD, pp. 7–18.

Kruskal, J.B., 1977. Three-way arrays: rank and uniqueness of trilinear decompositions, with application to arithmetic complexity and statistics. Linear Algebra Appl. 18, 95–138. doi:10.1016/0024-3795(77)90069-6.

Leonardi, N., Shirer, W.R., Greicius, M.D., Van De Ville, D., 2014. Disentangling dynamic networks: separated and joint expressions of functional connectivity patterns in time. Hum. Brain Mapp. 35, 5984–5995. doi:10.1002/hbm.22599.

Li, J., Choi, S., Joshi, A.A., Wisnowski, J.L., Leahy, R.M., 2020a. Temporal non-local means filtering for studies of intrinsic brain connectivity from individual resting fMRI. Med. Image Anal. 61, 101635. doi:10.1016/j.media.2020.101635.

Li, J., Choi, S., Joshi, A.A., Wisnowski, J.L., Leahy, R.M., 2018. Global PDF-based temporal non-local means filtering reveals individual differences in brain connectivity. In: IEEE 15th International Symposium on Biomedical Imaging, Washington, DC, pp. 15–19. doi:10.1109/ISBI.2018.8363513.

Li, J., Haldar, J.P., Mosher, J.C., Nair, D.R., Gonzalez-Martinez, J.A., Leahy, R.M., 2019a. Scalable and robust tensor decomposition of spontaneous stereotactic EEG data. IEEE Trans. Biomed. Eng. 66, 1549–1558. doi:10.1109/TBME.2018.2875467.

Li, J., Joshi, A.A., Leahy, R.M., 2020b. A network-based approach to study of ADHD using tensor decomposition of resting state fMRI data. In: IEEE 17th International Symposium on Biomedical Imaging. IEEE, Iowa City, IA, USA, pp. 1–5. doi:10.1109/ISBI45749.2020.9098584.

Li, J., Leahy, R.M., 2017. Parameter selection for optimized non-local means filtering of task fMRI. In: IEEE 14th International Symposium on Biomedical Imaging, Melbourne, Australia, pp. 476–480. doi:10.1109/ISBI.2017.7950564.

Li, J., Mosher, J.C., Nair, D.R., Gonzalez-Martinez, J., Leahy, R.M., 2017. Robust tensor decomposition of resting brain networks in stereotactic EEG. In: 51st Asilomar Conference on Signals, Systems, and Computers, Pacific Grove, CA, USA, pp. 1544–1548. doi:10.1109/ACSSC.2017.8335616.

Li, J., Wisnowski, J.L., Joshi, A.A., Leahy, R.M., 2021. Robust brain network identification from multi-subject asynchronous fMRI data. Neuroimage 227, 117615. doi:10.1016/j.neuroimage.2020.117615.

Li, J., Wisnowski, J.L., Joshi, A.A., Leahy, R.M., 2019b. Brain network identification in asynchronous task fMRI data using robust and scalable tensor decomposition. In: SPIE Medical Imaging 2019: Image Processing. Presented at the Image Processing, San Diego, United States, p. 22. doi:10.1117/12.2512684.

Liu, W., Kohn, N., Fernández, G., 2019. Intersubject similarity of personality is associated with intersubject similarity of brain connectivity patterns. Neuroimage 186, 56–69. doi:10.1016/j.neuroimage.2018.10.062.

Logothetis, N.K., Wandell, B.A., 2004. Interpreting the BOLD signal. Annu. Rev. Physiol. 66, 735–769. doi:10.1146/annurev.physiol.66.082602.092845.

Mishkin, M., Ungerleider, L.G., Macko, K.A., 1983. Object vision and spatial vision: two cortical pathways. Trends Neurosci. 6, 414–417. doi:10.1016/0166-2236(83)90190-X.

Murphy, K., Fox, M.D., 2017. Towards a consensus regarding global signal regression for resting state functional connectivity MRI. Neuroimage 154, 169–173. doi:10.1016/j.neuroimage.2016.11.052.

Nickerson, L.D., Smith, S.M., Öngür, D., Beckmann, C.F., 2017. Using dual regression to investigate network shape and amplitude in functional connectivity analyses. Front. Neurosci. 11. doi:10.3389/fnins.2017.00115.

Rabinovich, M.I., Friston, K.J., Varona, P., 2012. Principles of Brain Dynamics Global State Interactions. MIT Press, Cambridge, Mass.

Raichle, M.E., 2015. The brain's default mode network. Annu. Rev. Neurosci. 38, 433–447. doi:10.1146/annurev-neuro-071013-014030.

Raichle, M.E., Snyder, A.Z., 2007. A default mode of brain function: a brief history of an evolving idea. Neuroimage 37, 1083–1090. doi:10.1016/j.neuroimage.2007.02.041.

Riaz, A., Asad, M., Alonso, E., Slabaugh, G., 2020. DeepFMRI: end-to-end deep learning for functional connectivity and classification of ADHD using fMRI. J. Neurosci. Methods 335, 108506. doi:10.1016/j.jneumeth.2019.108506.

Robinson, E.C., Jbabdi, S., Glasser, M.F., Andersson, J., Burgess, G.C., Harms, M.P., Smith, S.M., Van Essen, D.C., Jenkinson, M., 2014. MSM: a new flexi-

ble framework for multimodal surface matching. Neuroimage 100, 414–426. doi:10.1016/j.neuroimage.2014.05.069.
Rockland, K.S., 2019. What do we know about laminar connectivity? Neuroimage 197, 772–784. doi:10.1016/j.neuroimage.2017.07.032.
Schaefer, A., Kong, R., Gordon, E.M., Laumann, T.O., Zuo, X.-N., Holmes, A.J., Eickhoff, S.B., Yeo, B.T.T., 2018. Local-global parcellation of the human cerebral cortex from intrinsic functional connectivity MRI. Cereb. Cortex 28, 3095–3114. doi:10.1093/cercor/bhx179.
Shattuck, D.W., Leahy, R.M., 2002. BrainSuite: an automated cortical surface identification tool. Med. Image Anal. 6, 129–142. doi:10.1016/S1361-8415(02)00054-3.
Sidiropoulos, N.D., Bro, R., 2000. On the uniqueness of multilinear decomposition of N-way arrays. J. Chemom. 14, 229–239. doi:10.1002/1099-128X(200005/06)14:3<229::AID-CEM587>3.0.CO;2-N.
Silbersweig, D., 2013. Default mode subnetworks, connectivity, depression and its treatment: toward brain-based biomarker development. Biol. Psychiatry 74, 5–6. doi:10.1016/j.biopsych.2013.05.011.
Smith, S.M., Beckmann, C.F., Andersson, J., Auerbach, E.J., Bijsterbosch, J., Douaud, G., Duff, E., Feinberg, D.A., Griffanti, L., Harms, M.P., Kelly, M., Laumann, T., Miller, K.L., Moeller, S., Petersen, S., Power, J., Salimi-Khorshidi, G., Snyder, A.Z., Vu, A.T., Woolrich, M.W., Xu, J., Yacoub, E., Uğurbil, K., Van Essen, D.C., Glasser, M.F., 2013. Resting-state fMRI in the human connectome project. Neuroimage 80, 144–168. doi:10.1016/j.neuroimage.2013.05.039.
Smith, S.M., Fox, P.T., Miller, K.L., Glahn, D.C., Fox, P.M., Mackay, C.E., Filippini, N., Watkins, K.E., Toro, R., Laird, A.R., Beckmann, C.F., 2009. Correspondence of the brain's functional architecture during activation and rest. Proc. Natl. Acad. Sci. 106, 13040–13045. doi:10.1073/pnas.0905267106.
Smith, S.M., Hyvärinen, A., Varoquaux, G., Miller, K.L., Beckmann, C.F., 2014. Group-PCA for very large fMRI datasets. Neuroimage 101, 738–749. doi:10.1016/j.neuroimage.2014.07.051.
Tagliazucchi, E., von Wegner, F., Morzelewski, A., Brodbeck, V., Laufs, H., 2012. Dynamic BOLD functional connectivity in humans and its electrophysiological correlates. Front. Hum. Neurosci. 6. doi:10.3389/fnhum.2012.00339.
ten Berge, J.M.F., Sidiropoulos, N.D., 2002. On uniqueness in candecomp/parafac. Psychometrika 67, 399–409. doi:10.1007/BF02294992.
The ADHD, 2012. The ADHD-200 Consortium: a model to advance the translational potential of neuroimaging in clinical neuroscience. Front. Syst. Neurosci. 6. doi:10.3389/fnsys.2012.00062.
Tomasi, G., Bro, R., 2005. PARAFAC and missing values. Chemometric. Intell. Lab. Syst. 75, 163–180. doi:10.1016/j.chemolab.2004.07.003.
Uddin, L.Q., Betzel, R.F., Cohen, J.R., Damoiseaux, J.S., De Brigard, F., Eickhoff, S., Fornito, A., Gratton, C., Gordon, E.M., Laird, A., Larson-Prior, L.J., McIntosh, A.R., Nickerson, L.D., Pessoa, L., Pinho, A.L., Poldrack, R., Razi, A., Sadaghiani, S., Shine, J.M., Yendiki, A., Yeo, B.T.T., Spreng, R.N., 2022. Controversies and current progress on large-scale brain network nomenclature from OHBM WHATNET: workgroup for HArmonized Taxonomy of NETworks (preprint). Open Sci. Framework doi:10.31219/osf.io/25za6.
Uddin, L.Q., Kelly, A.M.C., Biswal, B.B., Margulies, D.S., Shehzad, Z., Shaw, D., Ghaffari, M., Rotrosen, J., Adler, L.A., Castellanos, F.X., Milham, M.P., 2008. Network homogeneity reveals decreased integrity of default-mode network in ADHD. J. Neurosci. Methods 169, 249–254. doi:10.1016/j.jneumeth.2007.11.031.
Uddin, L.Q., Yeo, B.T.T., Spreng, R.N., 2019. Towards a universal taxonomy of macro-scale functional human brain networks. Brain Topogr. 32, 926–942. doi:10.1007/s10548-019-00744-6.
Van der Meer, T., Te Grotenhuis, M., Pelzer, B., 2010. Influential cases in multilevel modeling: a methodological comment. Am. Sociol. Rev 75, 173–178. doi:10.1177/0003122409359166.
Van Essen, D.C., Ugurbil, K., Auerbach, E., Barch, D., Behrens, T.E.J., Bucholz, R., Chang, A., Chen, L., Corbetta, M., Curtiss, S.W., Della Penna, S., Feinberg, D., Glasser, M.F., Harel, N., Heath, A.C., Larson-Prior, L., Marcus, D., Michalareas, G., Moeller, S., Oostenveld, R., Petersen, S.E., Prior, F., Schlaggar, B.L., Smith, S.M., Snyder, A.Z., Xu, J., Yacoub, E., 2012. The human connectome project: a data acquisition perspective. Neuroimage 62, 2222–2231. doi:10.1016/j.neuroimage.2012.02.018.
Welch, P., 1967. The use of fast Fourier transform for the estimation of power spectra: a method based on time averaging over short, modified periodograms. IEEE Trans. Audio Electroacoust. 15, 70–73. doi:10.1109/TAU.1967.1161901.
Xu, J., Potenza, M.N., Calhoun, V.D., Zhang, R., Yip, S.W., Wall, J.T., Pearlson, G.D., Worhunsky, P.D., Garrison, K.A., Moran, J.M., 2016. Large-scale functional network overlap is a general property of brain functional organization: reconciling inconsistent fMRI findings from general-linear-model-based analyses. Neurosci. Biobehav. Rev. 71, 83–100. doi:10.1016/j.neubiorev.2016.08.035.
Yeo, B.T.T., Krienen, F.M., Chee, M.W.L., Buckner, R.L., 2014. Estimates of segregation and overlap of functional connectivity networks in the human cerebral cortex. Neuroimage 88, 212–227. doi:10.1016/j.neuroimage.2013.10.046.
Yeo, B.T.T., Krienen, F.M., Sepulcre, J., Sabuncu, M.R., Lashkari, D., Hollinshead, M., Roffman, J.L., Smoller, J.W., Zöllei, L., Polimeni, J.R., Fischl, B., Liu, H., Buckner, R.L., 2011. The organization of the human cerebral cortex estimated by intrinsic functional connectivity. J. Neurophysiol. 106, 1125–1165. doi:10.1152/jn.00338.2011.
Yeo, B.T.T., Sabuncu, M.R., Vercauteren, T., Ayache, N., Fischl, B., Golland, P., 2010. Spherical demons: fast diffeomorphic landmark-free surface registration. IEEE Trans. Med. Imaging 29, 650–668. doi:10.1109/TMI.2009.2030797.
Zhang, T., Li, C., Li, P., Peng, Y., Kang, X., Jiang, C., Li, F., Zhu, X., Yao, D., Biswal, B., Xu, P., 2020. Separated channel attention convolutional neural network (sc-cnn-attention) to identify ADHD in multi-site rs-fMRI dataset. Entropy 22, 893. doi:10.3390/e22080893.
Zou, L., Zheng, J., Miao, C., Mckeown, M.J., Wang, Z.J., 2017. 3D CNN based automatic diagnosis of attention deficit hyperactivity disorder using functional and structural MRI. IEEE Access 5, 23626–23636. doi:10.1109/ACCESS.2017.2762703.